2015

First-principles and Many-Body Methods: Implementations and Applications to Study Spintronic Materials

Ryky Nelson
Louisiana State University and Agricultural and Mechanical College, rnels12@lsu.edu

FIRST-PRINCIPLES AND MANY-BODY METHODS: IMPLEMENTATIONS AND APPLICATIONS TO STUDY SPINTRONIC MATERIALS

A Dissertation

Submitted to the Graduate Faculty of the
Louisiana State University and
Agricultural and Mechanical College
in partial fulfillment of the
requirements for the degree of
Doctor of Philosophy

in

The Department of Physics and Astronomy

by
Ryky Nelson
B.Sc., University of Indonesia, 2007
December 2015

Acknowledgments

First I would like to thank my advisor, Juana Moreno who has allowed me to pursue my Ph.D. degree in computational condensed matter physics and for her support, knowledge, and guidance during my Ph.D. study. I would also like to thank Mark Jarrell and Wei Ku for valuable discussion and guidance that help me broaden my knowledge of physics and research. I also want to thank my graduate advisory committee, Juana Moreno, Mark Jarrell, Wei Ku, Pedro Derosa, Richard Kurtz, and Karen Luttrell for serving on my committee. Special thanks to Tom Berlijn for all insightful discussions and advice. I also want to thank Carol Duran for her valuable assistance. Finally, I would like to thank all my colleagues Shuxiang Yang, Peter Reis, Kalani Hettiarachchilage, Kuang-Shing Chen, Peng Zhang, Xiaoyao Ma, Kiran B. Nair, Ka-Ming Tam and others for their help and support during all my Ph.D. years.

Table of Contents

Abstract

Diluted magnetic semiconductors (DMSs) and magnetoresistive materials are instrumental for the development of spintronic technology. Before we are able to engineer spintronic devices, it is necessary to understand the properties of materials from which spintronic devices are made, otherwise time and other resources will be wasted.

In this thesis, we investigate some aspects of diluted magnetic semiconductors and a magnetoresistive material Ta_2PdSe_6 with first-principle and many-body methods. Particularly, we investigate the Mn valence in (Ga,Mn)N and derive low-energy models of (Ga,Mn)N by making use of a first-principles Wannier-function analysis. Additionally, we also study the disorder-driven localization in DMSs with the typical-medium theory (TMT). Finally, we present a discussion about the investigation of the mechanism behind Ta_2PdSe_6 magnetoresistance.

From a first-principles Wannier-function analysis, we find unambiguously the Mn valence in (Ga,Mn)N to be close to 2+ (d^5), but in a mixed spin configuration with average magnetic moments of $4\mu_B$. By integrating out high-energy degrees of freedom differently, we further derive for the first time from first-principles two low-energy pictures that reflect the intrinsic dual nature of the doped holes in the (Ga,Mn)N: 1) an effective d^4 picture ideal for local physics, and 2) an effective d^5 picture suitable for extended properties. Furthermore, our results further reveal a few novel physical effects and pave the way for future realistic studies of magnetism. Our study not only resolves one of the outstanding key controversies of the field, but also exemplifies the general need for multiple effective descriptions to account for the rich low-energy physics in many-body systems in general.

Meanwhile, by implementing a geometrical average of the local density of states to define an order parameter, the typical density of states (TDOS), we find that the TDOS vanishes below a critical doping concentration, indicating an Anderson localization tran-

sition in the system. Our results qualitatively explain why at concentrations lower than a critical value DMSs are insulating and non-magnetic, whereas at larger concentrations they are ferromagnetic bad metals.

On the investigation of Ta_2PdSe_6, our density functional theory (DFT) calculations show that the material is a semimetal that has two types of charge carriers with the same density. This result, together with the magnetoresistance behavior of the two-band model, leads to the conclusion that the mechanism responsible for Ta_2PdSe_6 magnetoresistance is charge compensation.

Chapter 1
Introduction

A new paradigm in electronics based on the use of the spin degree of freedom instead of or in addition to the charge degree of freedom has emerged a few decades ago. The field of spintronics began with the discovery of the giant magnetoresistive (GMR) effect [1]. GMR is observed when a nonmagnetic metal layer is sandwiched by two magnetic layers in which one has a fixed magnetization and the magnetization of the other layer can be modified with an external field. The resistance of the metal is lowest when the magnetization of the two layers is aligned and highest when opposite. Now GMR is widely implemented for read heads in hard drives with the density approaching 19 Gbits/cm^2 [2] and magnetic sensors [3, 4]. Soon after the GMR discovery scientists realized more potential applications of spintronics such as nonvolatile memories [5, 6], which allow a possible integration of data processing and storage into one electronic component, spin-generating solar cells [7, 8], electrical spin injection [9], spin-LED (light-emitting diode) [10], and electrically or optically controlled ferromagnets [11]. These applications, however, need the integration of charge and spin degrees of freedom.

To produce spintronics we need (ferro-)magnetic materials in the first place. Ferromagnetic metals are still common materials to make spintronic devices. However, metal-based spintronic devices have a disadvantage when combined with semiconductors, namely a metal-semiconductor junction always produces a Schottky barrier that reduces spin lifetimes. Scientists are still trying to improve the spin injection methods from ferromagnetic metals to semiconductors [10], while other ferromagnetic materials better matched with semiconductor components are being developed. Other candidates for spintronic materials include ferromagnetic oxides and Heusler alloy [12, 13, 14]. However, the problem with these materials is that they produce high spin polarization only at low temperature [10].

How about magnetic semiconductors themselves? Unfortunately, most semiconductors, especially those conventional semiconductors developed for present electronics, are not ferromagnetic. The earliest studied magnetic semiconductors are Eu chalcogenides [15, 16] and chromium spinels [17]. Scientists have found that the carriers in these materials interact strongly with the magnetic subsystem and thus the concentration of the carriers greatly affects Curie temperature (T_c) in these materials; T_c of EuO, for instance, is enhanced from 69 to 136 K [16] when doped with Gd. Unfortunately, the problems of synthesizing heterostructures of these materials have caused the community to lose interest in further developing these compounds. A recent observation that shows nearly fully polarized doped carriers in EuO [18] has renewed the interest in developing Eu chalcogenides as a potential spin-polarized carriers injector [19].

Another method scientists have tried to induce magnetism in semiconductors is doping. Just like the doping method used to manipulate the electronic properties of semiconductors, now, with the same hope, scientists use doping to engineer magnetic semiconductors. The most intuitive doping method is by low-doping semiconductors with magnetic impurities, such as transition metals, i.e. diluted magnetic semiconductors (DMSs). The test on silicon was not promising since the produced (Si, Mn) samples consist of two phases, a ferromagnetic phase with $T_c \approx 30$ K and an antiferromagnetic phase in the form of clusters with $T_N \approx 95$ K [20]. Scientists have also tried this method for II-VI [21] and IV-VI [22] semiconductors by alloying them with magnetic ions. These materials are often called semimagnetic semiconductors [20] since dopants only provide local magnetic moments whereas carriers are provided by other doping. While doped IV-VI DMSs show ferromagnetism the compounds and their heterostructures are hard to synthesize [20]. Moreover, the antiferromagnetic interaction between magnetic atoms in II-VI DMSs, unfortunately, is too strong, thus suppressing T_c [23, 20]. Another interesting semiconductor family is the III-V semiconductors. Transition metal dopants in these semiconductors randomly substitute the cations up to a given percentage. One of the advantages of these DMSs is that the metal

dopant not only provides local moments but also carriers. The host crystal is also optically active, and thus it holds the potential for integrated magneto-optical devices [24, 25].

The most widely studied III-V DMSs is (Ga,Mn)As. The earliest synthesis of (Ga,Mn)As was by Ohno's group [26], who successfully grew homogeneous (Ga,Mn)As samples using the low-temperature molecular-beam epitaxy (LT-MBE) technique. The samples exhibited ferromagnetism, albeit with a low T_c. Since then other groups have investigated this material experimentally and theoretically. Some further experimental studies [9, 25, 27], for instance, yield data that lead to the theory of a carrier-mediated exchange mechanism in this material. This model has predicted many (Ga,Mn)As properties [28, 29, 30]. First-principles-based studies [31, 32] also have been performed to explore the electronic structure of this DMS. Now, scientists in this community agree that the dominant mechanism responsible for ferromagnetism in (Ga,Mn)As is the carrier-mediated exchange. However, there are some other mechanisms and factors [33], such as Mn-Mn antiferromagnetic super-exchange and interstitial Mn and disorder effects that affect T_c and need further investigation to improve the properties of (Ga,Mn)As. Although researchers have started to use this material for electronic applications [34], there is still much to investigate about this material at the level of basic and applied research.

Another III-V semiconductor of considerable interest is (Ga,Mn)N. One of the motivations is that the blue LED technology [35, 36, 37] is based on the host compound GaN. (Ga,Mn)N also might be instrumental toward the realization of efficient spintronic devices. Dietl *et al.* [28] predicted its T_c to be above room temperature; a feature which is obviously required in order to be technologically advantageous. However, until now this prediction remains far from being fulfilled as various experiments lead to controversial conclusions concerning the ferromagnetism in (Ga,Mn)N. Chen *et al.* [38] detected superparamagnetism in their nanocluster (Ga,Mn)N sample, while Zając *et al.* [39] and Granville *et al.* [40] report antiferromagnetic coupling between Mn ions in their sample. Interestingly, Dhar *et al.* [41] in their investigation observe a Heisenberg spin-glass with a transition temperature around

4.5 K. Observations of the desired ferromagnetic ordering, on the other hand, have also been reported, albeit with fiercely varying T_c's; some [42, 43] find low T_c's between 10 K and 25 K, while others [44, 45] report ferromagnetism around room temperature or higher [46].

One factor considered to be instrumental for the magnetic order and the coupling mechanism in DMSs is the valence state of Mn [33, 47, 48]. There is no doubt that in addition to a local moment, a (Ga,Mn) substitution injects a hole into the system, but the question is: where is this hole located? If the hole resides mostly in the N valence bands it is likely to be delocalized, resulting in a Mn valence of $2+(d^5)$. In this case, similar to (Ga,Mn)As systems [28, 49], the microscopic mechanism is described by pictures of Zener's kinetic-exchange type [50], in which the coupling between local moments is mediated by valence-band itinerant carriers. This mechanism has been examined experimentally for $Ga_{1-x}Mn_xAs$ [9, 51, 52, 53, 54]. If, on the other hand, the hole resides mostly in Mn ions, the Mn valence is $3+(d^4)$, and the magnetic coupling would be better described by a double-exchange mechanism [55, 56] mediated by impurity levels [57, 48].

Another aspect of DMSs that is very interesting to study is the carrier localization. As mentioned previously, excess carriers that are created in DMSs by doping can help to mediate the interaction between local spins. This mediation, however, depends on the actual behavior of the carriers. If the carriers are localized they are unlikely to mediate a long-range interaction, and thus the system would end up non-magnetic. If, on the other hand, the carriers are delocalized, the local spins in the system can have a long-range interaction with each other through carrier mediation. This long-range interaction would bring the system into a magnetic order. Some experimental studies [58] have shown the tendency of DMS systems to have Anderson-localization transition at very low doping. However, no previous theoretical studies have demonstrated Anderson-localization in DMSs. As will be shown in detail in this report, another method called typical-medium theory is needed to demonstrate this localization in DMSs.

GMR materials have been critical for spintronics. However, many materials especially metals also display magnetoresistance. The ordinary magnetoresistive effect was first discovered in nickel and iron by W. Thomson in 1856 [59]. Later scientists found different mechanisms to produce large magnetoresistance. One of the mechanisms is to use multiple components as implemented for GMR. The other mechanism is intrinsic and called the double-exchange mechanism which was originally proposed to explain colossal magnetoresistance in perovskite manganese [60]. A relatively new material, Ta_2PdSe_6, is found to have large magnetoresistance [61]. However, the mechanism is still unknown. Therefore, a theoretical study is needed to determine its magnetoresistance mechanism. The results of this study will perhaps encourage further studies of this material.

This work is aimed at studying magnetic and electronic properties of DMSs and magnetoresistive materials through first-principles and many-body methods. First-principles method will first be reviewed in Chapter 2. Next, we review in Chapter 3 effective Hamiltonians and mean-field methods used to study DMSs. In Chapter 4, we discuss in detail first-principles analysis of the valence of Mn in (Ga,Mn)N and low-energy pictures of (Ga,Mn)N. Anderson localization in DMSs will be discussed in Chapter 5 and the first-principles description of Ta_2PdSe_6 magnetoresistance will be discussed in Chapter 6. Finally, we summarize in Chapter 7.

Chapter 2
First-Principles Methods

This chapter describes the density functional theory (DFT) and an ab-inito downfolding method used in this work. The DFT is commonly used to study semiconductors and can be traced back to the Thomas-Fermi model. The first-principles downfolding method presented in this work is a means to obtain low energy pictures of systems of interest by projecting Wannier functions onto Bloch states.

2.1 Density Functional Theory

We start from the well-known Hamiltonian describing the motion of electrons in the vicinity of a lattice of positive charged nuclei that are approximately treated as an external potential:

$$H = -\frac{\hbar}{2m_e}\sum_i \nabla_i^2 - \sum_{i,j}\frac{Z_j e^2}{|\mathbf{R}_j - \mathbf{r}_i|} + \sum_{i<j}\frac{e^2}{|\mathbf{r}_j - \mathbf{r}_i|}\ , \tag{2.1}$$

where Z_j denotes the nucleus charge whereas $\mathbf{R}_j$ and $\mathbf{r}_i$, respectively, denote the position of nuclei j and electron i. In order to get the properties of the system, one needs to solve the corresponding Schrödinger equation:

$$H\Psi\left(\mathbf{r}_1 \ldots \mathbf{r}_N\right) = E\Psi\left(\mathbf{r}_1 \ldots \mathbf{r}_N\right) \tag{2.2}$$

As can be realized immediately, the N-electron problem (where $N \sim 10^{23}$) is impossible to solve analytically or even numerically with current computers; the problem we are facing is a second-order partial differential equation with $3N$ degrees of freedom (excluding spin).

2.1.1 Hohenberg-Kohn Theorems

The complexity of Equation (2.2) can be simplified if one reformulates it in terms of the electron density. In this way, we only deal with 3 (instead of $3N$) degrees of freedom. This approach is known as the density functional theory (DFT). Hohenberg and Kohn have shown through their theorems that this formulation is possible. Their first theorem states that any system's ground-state density $n(\mathbf{r})$ uniquely determines the external potential applied to the system. To prove this theorem we apply two different potentials, $v_1(\mathbf{r})$ and $v_2(\mathbf{r})$ to a system (the system is assumed to have a non-degenerate ground state although it is not restricted). The potentials, respectively, correspond to Hamiltonian H_1 and H_2 and result in the ground states $|1\rangle$ and $|2\rangle$ which have the same ground state density $n_0(\mathbf{r})$. If we consider

$$E_1 = \langle 1|H_1|1\rangle < \langle 2|H_1|2\rangle \ , \tag{2.3}$$

and

$$E_2 = \langle 2|H_2|2\rangle < \langle 1|H_2|1\rangle \ . \tag{2.4}$$

Since $H_1 - H_2 = \hat{v}_1 - \hat{v}_2$ we have

$$\langle 2|H_1|2\rangle \ = \langle 2|H_2|2\rangle + \int d\mathbf{r}\, (v_1(\mathbf{r}) - v_2(\mathbf{r}))\, n_0(\mathbf{r}) \ , \tag{2.5}$$

or in other words

$$E_1 < E_2 + \int d\mathbf{r}\, (v_1(\mathbf{r}) - v_2(\mathbf{r}))\, n_0(\mathbf{r}). \tag{2.6}$$

By exchanging index 1 and 2, we can also show

$$E_2 < E_1 + \int d\mathbf{r}\, (v_2(\mathbf{r}) - v_1(\mathbf{r}))\, n_0(\mathbf{r}). \tag{2.7}$$

Adding (2.6) and (2.7) results in a contradiction: $E_1 + E_2 < E_2 + E_1$ and, thus, proves the theorem. Furthermore, since there is only a unique external potential $v(\mathbf{r})$ defined by the

corresponding density n, there exists, in principle, an energy functional associated with the potential:

$$E[n] = F[n] + v[n] \ ; \ v[n] \equiv \int d\mathbf{r} \ v(\mathbf{r}) \ n(\mathbf{r}) \ . \tag{2.8}$$

Here, $F[n]$ is the universal functional that consists of the kinetic and electron-electron interaction terms.

To complete the formulation, the second Hohenberg-Kohn theorem shows that the energy functional $E[n]$ corresponding to the external potential $v(\mathbf{r})$ is globally minimized by the ground state density $n_0(\mathbf{r})$. This can be easily proved by first noting that all properties including the ground state Ψ_0 are uniquely determined by the external potential. Since the external potential itself is uniquely determined by the ground state density, so is $F[n]$. Thus, by definition the energy functional will be globally minimized by the ground state density constructed directly from the ground state. These two theorems are the foundation of DFT that greatly simplify the many-electron problem.

2.1.2 Kohn-Sham Equations

Despite the significant breakthrough made by Hohenberg-Kohn theorems, an additional approximation is, however, needed to make DFT useful since the exact form of $F[n]$ is unknown. The approach is to consider, as an auxiliary system, the non-interacting system which has the same ground state density as the interacting system's density, $n_0(\mathbf{r})$. The energy functional of the non-interacting system is given by:

$$E_s[n] = T_s[n] + v_s[n] \tag{2.9}$$

where $T_s[n]$ is the kinetic energy functional and v_s the external potential of the non-interacting system that produces $n_0(\mathbf{r})$. In this way the exchange-correlation energy func-

tional E_{xc} and potential v_{xc} can be defined as:

$$E_{xc}[n] \equiv F[n] - E_H[n] - T_s[n] \; ; v_{xc}(\mathbf{r}) = \frac{\delta E_{xc}[n]}{\delta n} \; , \tag{2.10}$$

and the Hartree term is given by

$$E_H[n] = \frac{1}{2} \int \int d\mathbf{r} \; d\mathbf{r}' \; n(\mathbf{r}) \; \frac{e^2}{|\mathbf{r} - \mathbf{r}'|} \; n(\mathbf{r}') \; . \tag{2.11}$$

By minimizing the energy functionals (2.8) and (2.9) with respect to their ground state density, we can get:

$$v_s(\mathbf{r}) = v(\mathbf{r}) + \int d\mathbf{r}' \; \frac{e^2 n(\mathbf{r}')}{|\mathbf{r} - \mathbf{r}'|} \; + v_{xc}(\mathbf{r}) \; . \tag{2.12}$$

The approach, furthermore, is completed by expressing the ground state density in terms of single-particle orbitals:

$$n(\mathbf{r}) = \sum_{i=1}^{N} |\phi_i(\mathbf{r})|^2 \; , \tag{2.13}$$

and the non-interacting problem (2.9) as

$$H_{KS} \; \phi_i(\mathbf{r}) = \left[-\frac{\hbar}{2m_e} \nabla^2 + v_s(\mathbf{r}) \right] \phi_i(\mathbf{r}) = \varepsilon_i \; \phi_i(\mathbf{r}) \; . \tag{2.14}$$

One now only needs to solve self-consistently equations (2.14) and (2.13) which are known as the Kohn-Sham (KS) equations. The DFT package we use for our project is WIEN2K [76].

2.1.3 Density Functional Theory Exchange-Correlation Potentials

Since the exchange-correlation potential $v_{xc}(\mathbf{r})$ cannot be determined exactly further approximations are needed in order to put DFT into practice. Today, people have derived many approximate forms of $v_{xc}(\mathbf{r})$. The earliest and widely-used approximation is the local density approximation (LDA) $v_{xc}(\mathbf{r})$. The idea behind this approximation is to express the

exchange-correlation energy as a function of the local density:

$$E_{xc}^{LDA}[n] = \int d\mathbf{r}\ \epsilon_{xc}(n)\ n(\mathbf{r})\ ;\ \epsilon_{xc}(n) = \epsilon_x(n) + \epsilon_c(n)\ . \tag{2.15}$$

Here, the exchange energy is approximated by the exchange energy of the homogeneous electron gas (HEG) which is known analytically:

$$\epsilon_x(n) = -\frac{3}{4}\left(\frac{3}{\pi}\right)^{1/3} n^{1/3}(\mathbf{r})\ , \tag{2.16}$$

whereas the correlation energy is produced through fitting of a correlation functional, like Perdew-Zunger [62] or Vosko-Wilk-Nusair [63], to Monte Carlo results [64]. The LDA can be generalized to local spin density approximation (LSDA) by explicitly considering the exchange-correlation energy as a function of spin-up and -down electron densities:

$$E_{xc}^{LSDA} = \int d\mathbf{r}\ \epsilon_{xc}(n_\uparrow, n_\downarrow)\ n(\mathbf{r})\ . \tag{2.17}$$

LDA (LSDA) has become very popular because it predicts properties of many materials remarkably well, especially non-correlated materials like semiconductors and simple metals.

Although LDA has been very good in describing many materials, its accuracy can still be improved by considering how the density varies in materials. This makes sense since in real materials the density can vary so rapidly such that LDA fails to capture this density variation. Therefore, the first reasonable correction that can be made to LDA would be to consider the gradient of the density. This approximation that is known as the generalized-gradient approximation (GGA) [65, 66, 67, 68] has been widely used to substitute or to complement LDA in studying electronic structure. In one of our projects we implement the GGA of Perdew-Burke-Ernzerhof for solids (PBESOL) [68].

Another DFT that we use in our project is called modified Becke-Johnson potential. The potential was introduced by F. Tran and P. Blaha [69] by modifying the potential that

was originally proposed by A. D. Becke and E. R. Johnson [70]. The potential is aimed to improved the band gap of semiconductors and insulators that is always underestimated by LDA. The results of the potential are very impressive due to its capability to give more accurate band gaps while keeping the calculation cheap compared to the *GW* method [76].

Despite the improvement of the accuracy of the potential, there are some other materials like transition metals and their oxides that cannot be described at all by LDA and other orbital-independent DFT exchange-correlation potentials. This class of materials is called strongly-correlated materials. Most of them consist of elements with d or f orbitals. These orbitals are quite localized, thus the electron-electron (Hubbard) interaction U is comparable to their kinetic energy and causes strong correlations between electrons. Fortunately, to some extent, LDA can be improved to include U in the calculation. The idea of LDA+U is to group orbitals into two types; those which have strong U and the rest. To the former we apply an *ad hoc* U, thus our energy functional now becomes

$$E^{\mathrm{LDA}+U}[n] = E^{\mathrm{LDA}}[n] + E^{U}[n] - E^{\mathrm{dc}}[n] \ , \tag{2.18}$$

where $E^{U}[n]$ is the energy functional in which we explicitly set U in localized orbitals, whereas $E^{\mathrm{dc}}[n]$ is the "double-counting" term we need to subtract since $E^{\mathrm{LDA}}[n]$ has already included the mean-field value of U in the standard DFT procedure. The U itself can be determined self-consistently through a constrained calculation or treated as an adjustable parameter. Several ways to determine $E^{U}[n]$ and $E^{\mathrm{dc}}[n]$ can be found in References [71, 72, 73]. To study the valence of Mn in (Ga,Mn)N we implement LDA+U as formulated in [72] to appropriately treat the Mn d orbital.

2.1.4 Linearized Augmented Plane Waves

In order to solve the Kohn-Sham equations we need to expand the eigenstates in a complete, but not necessarily orthogonal, basis set: $\sum_i |a_i\rangle\langle a_i| = 1$. Using this particular basis set,

the KS equation (2.14) now forms the secular equation:

$$|H_{ij} - \varepsilon_i S_{ij}| = 0 \tag{2.19}$$

where $H_{ij} = \langle a_i | H_{KS} | a_j \rangle$ and $S_{ij} = \langle a_i | a_j \rangle$.

One of the common basis sets used to solve the KS equation is the linearized augmented plane waves (LAPW) set. To describe LAPW, we first need to discuss another basis set called the augmented plane waves (APW) [74] which was formulated before LAPW. In the formulation of APW two kinds of regions are first defined: one is called the muffin-tin region (S_α) covering core electrons around nuclei and the other is called the interstitial region (I) covering valence electrons moving between the atoms. In the former region one uses a combination of atomic orbitals to describe the electronic wavefunction whereas in the latter region plane waves are used. This formulation is reasonable since Bloch states behave like atomic orbitals close to nuclei, due to diverging Coulomb interaction, whereas in the interstitial, where the interaction is weak, Bloch states behave as plane waves. Mathematically APW is given by:

$$\phi^{APW}_{\mathbf{G},\mathbf{k}}(\mathbf{r}, E) = \begin{cases} \sum_{l,m} A^{\mathbf{k}+\mathbf{G}}_{\alpha lm} u_{\alpha l}(\mathbf{r}, E) Y_{lm}(\hat{\mathbf{r}}) \ ; & \mathbf{r} \in S_\alpha \\ \frac{1}{\sqrt{V}} e^{i(\mathbf{k}+\mathbf{G}).\mathbf{r}} \ ; & \mathbf{r} \in I \ . \end{cases} \tag{2.20}$$

Here, $u_{\alpha l}(\mathbf{r}, E)$ and $Y_{lm}(\hat{\mathbf{r}})$, respectively, represent radial and spherical solutions of the KS equations. Coefficients $A^{\mathbf{k}+\mathbf{G}}_{\alpha lm}$ are determined such that the APW are continuous at the muffin-tin boundary. Although E in (2.20) is a continuous parameter, the closeness of its value to a given eigenvalue determines the quality of the basis. This makes the problem eigenvalue-dependent; thus non-linear, which is hard to solve, and becomes a disadvantage of this basis. To deal with the eigenvalue-dependence, O. K. Andersen [75] came up with the idea of expanding the radial solutions up to the first order correction, and thus linearizing

the basis set:

$$u_{\alpha l}(\varepsilon_i, \mathbf{r}) = u_{\alpha l}(E, \mathbf{r}) + \dot{u}_{\alpha l}(E, \mathbf{r})(\varepsilon_i - E) + \mathcal{O}(\varepsilon_i - E)^2 \ . \tag{2.21}$$

With this expansion, the solutions are still accurately calculated even when E is not so close to an eigenvalue. Formally, LAPW is given by:

$$\phi^{LAPW}_{\mathbf{G},\mathbf{k}}(\mathbf{r}, E) = \begin{cases} \sum_{l,m} \left[A^{\mathbf{k}+\mathbf{G}}_{\alpha lm} u_{\alpha l}(\mathbf{r}, E) + B^{\mathbf{k}+\mathbf{G}}_{\alpha lm} \dot{u}_{\alpha l}(\mathbf{r}, E) \right] Y_{lm}(\hat{\mathbf{r}}) \ ; & \mathbf{r} \in S_\alpha \\ \frac{1}{\sqrt{V}} e^{i(\mathbf{k}+\mathbf{G}).\mathbf{r}} \ ; & \mathbf{r} \in I \ . \end{cases} \tag{2.22}$$

Coefficients $A^{\mathbf{k}+\mathbf{G}}_{\alpha lm}$ and $B^{\mathbf{k}+\mathbf{G}}_{\alpha lm}$ are determined such that LAPW are continuous and smooth at the muffin-tin boundary. This basis set is one of the basis sets implemented in WIEN2K and used for our project.

2.2 Downfolding Method

Often we want to do calculations beyond the standard DFT but based on DFT calculations such as disorder calculations [77, 78] and/or including many-body effects [79, 80]. These calculations are usually implemented only for some relevant bands that are close to the Fermi energy ($\mathrm{E_F}$). Therefore, it is necessary to first "separate" these particular bands from the rest and construct the tight-binding Hamiltonian associated with these bands. The method to extract some particular bands from the entire Hilbert space is called downfolding.

The downfolding method implemented in this study uses Wannier-functions as the basis set to represent the tight-binding Hamiltonian. Wannier functions are defined as the Fourier transform of the Bloch states into the real space:

$$|rm\rangle = N^{-1/2} \sum_{\mathbf{k}j} e^{-i\mathbf{k}\cdot\mathbf{r}} \ U^{\mathbf{k}}_{jm} \ |\mathbf{k}j\rangle \ . \tag{2.23}$$

Here N denotes the number of unit cells in the system and $U^{\mathbf{k}}_{jm}$ is a unitary matrix which

plays the role of a gauge field and can be chosen freely. One method to determine this gauge is called maximally localized Wannier functions [81]. This approach minimizes the spread of the Wannier functions. For our study, the gauge is determined using the projected Wannier-functions method [79, 82].

The method we use to construct the Wannier functions is based on the algorithm described in Reference [82]. This Wannier-functions formulation has been implemented to study real materials [83, 84, 85, 86, 77, 78]. First, we construct projections of local orbitals $|\phi_m\rangle$ onto Bloch states: $\sum_j |\mathbf{k}j\rangle\langle\mathbf{k}j|\phi_m\rangle$. These projections cannot be directly Fourier transformed to get Wannier functions since they are not orthonormal. To orthonormalize them we exploit the gauge freedom $U^{\mathbf{k}}_{jm}$ in (2.23) according to Lödwin's symmetric orthonormalization prescription [87]:

$$U^{\mathbf{k}}_{jm} = \sum_{m'} \langle \mathbf{k}j|\phi_{m'}\rangle M_{m'm}(\mathbf{k}) \ , \tag{2.24}$$

where

$$M^{-2}_{m'm}(\mathbf{k}) = \left(\sum_{j'} \langle \phi_{m'}|\mathbf{k}j'\rangle\langle \mathbf{k}j'| \right) \sum_j |\mathbf{k}j\rangle\langle\mathbf{k}j|\phi_m\rangle = \sum_j \langle\phi_{m'}|\mathbf{k}j\rangle\langle\mathbf{k}j|\phi_m\rangle \ . \tag{2.25}$$

Now the projections $\sum_{jm'} |\mathbf{k}j\rangle\langle\mathbf{k}j|\phi_{m'}\rangle M_{m'm}(\mathbf{k})$ are orthonormal. In WIEN2K, the Bloch states can be represented using LAPW. The local orbitals, furthermore, are chosen according to the character of the bands which WIEN2K can help to determine.

Having formulated our Wannier functions, we can express our tight-binding Hamiltonian in the Wannier-functions basis:

$$\langle \mathbf{r}'m'|H_0|0m\rangle = \sum_{kj} \langle \mathbf{r}'m'|\mathbf{k}j\rangle \ \varepsilon_{kj} \ \langle \mathbf{k}j|0m\rangle \ . \tag{2.26}$$

Here the rotation matrix is given by (2.23) and (2.24)

$$\langle \mathbf{r}'m'|\mathbf{k}j\rangle = N^{-1/2} e^{i\mathbf{k}\cdot\mathbf{r}} \ \sum_{m'} \langle \mathbf{k}j|\phi_{m'}\rangle M_{m'm}(\mathbf{k}) \ . \tag{2.27}$$

Chapter 3
Mean-Field Methods

The first-principles methods described in the previous chapter are very good to describe properties of materials that usually do not involve many-body and/or disorder effects. In order to address these effects people usually take a different approach by using many-body techniques. Unlike first-principles methods that use a very large Hilbert space, many-body approaches usually use a Hamiltonian model that only covers the low-energy states of the system of interest. Once the model is determined one must decide on the many-body method to be used. The solutions are typically described in terms of Green functions.

In this chapter we are going to discuss a many-body method that can be used to described disorder-induced localization in diluted magnetic semiconductors (DMSs). We are first going to describe the model we use and how it is solved within a many-body method called the dynamical mean-field theory. At the end of this chapter, we are going to show how we can "reshape" the dynamical mean-field theory so that it is capable of capturing the Anderson localization transition in disorder systems.

3.1 Spin-Fermion Model

To model the dynamics of carriers in the vicinity of randomly distributed local spins, one implements the spin-fermion model which describes how the carriers move around under the influence of the potential created by the impurities, i.e. the local spins. Although there are various versions of the spin-fermion model, generally this model has two terms; the kinetic term of the carriers H_K and the exchange term describing the interaction between the carriers and local spins:

$$H = H_K - J_H \sum_i \mathbf{S}_i \cdot \boldsymbol{\sigma} \ . \tag{3.1}$$

The kinetic term can have various forms; from the simplest one which only considers nearest-neighbor hoppings to more complicated and general forms which consider, for instance, distant-neighbor hoppings and also other effects like spin-orbit couplings. However, the kinetic term is the periodic term that in principle can be solved exactly. The real complication comes from the second term which is a random potential. Therefore in order to solve it we need a method beyond the standard DFT where disorder averaging is considered.

One of the objectives of this study is to derive parameters for H_K and the exchange term by means of the Wannier function-based first-principles method as described in the previous chapter.

3.2 Dynamical Mean-Field Theory

Many models in physics often can be solved with mean-field methods. One of the mean-field methods used to solve many-body and/or disorder problems is the dynamical mean-field theory (DMFT). The idea of DMFT is to map the system of interest into an impurity model, very often into the single-impurity Anderson model (SIAM) [88], and consider temporal fluctuations which are excluded in the static mean-field theory. The spatial fluctuations, however, are ignored. Accordingly, the lattice self-energy is approximated by the impurity-site self-energy $\Sigma(\mathbf{k}, i\omega_n) \approx \Sigma_{impurity}(i\omega_n)$. It is worth noting that DMFT becomes exact in the limit of infinite spatial dimensions. After the mapping, the system now consists of two parts: an impurity site and an electron bath; an electron then can jump back and forth from the bath to the impurity site through a hybridization function that couples the bath and the impurity site.

This section describes specifically the implementation of DMFT for the spin-fermion model as described in Reference [56], whereas the details of the original derivation of DMFT can be found in References [89, 90]. In the spin-fermion model, the effective action is given

by:

$$S_{eff} = -\int_0^\beta \int_0^\beta \, d\tau_1 \, d\tau_2 \, c^\dagger(\tau_1) \, \mathcal{G}(\tau_1 - \tau_2) \, c(\tau_2) - J_H \int_0^\beta \, d\tau \, \mathbf{S} \cdot c^\dagger(\tau) \, \boldsymbol{\sigma} \, c(\tau) \, , \quad (3.2)$$

where $c^\dagger = (c_\uparrow^\dagger, c_\downarrow^\dagger)$ are Grassmann variables in the spinor notation. The DMFT algorithm is summarized as the following:

1. We start from a guessed self-energy and then calculate the local Green function G_{loc} by coarse-graining the lattice Green function:

$$G_{loc}(i\omega_n) = \frac{1}{N} \sum_{\mathbf{k}} \frac{1}{i\omega_n - (\varepsilon_{\mathbf{k}} - \mu) - \Sigma(i\omega_n)} = \int d\varepsilon \frac{DOS_0(\varepsilon)}{i\omega_n - (\varepsilon - \mu) - \Sigma(i\omega_n)} \, . \quad (3.3)$$

   Here $DOS_0(\varepsilon)$ is the bare density of state.

2. Next, the mean-field is obtained through the Dyson's equation:

$$\mathcal{G}(i\omega_n)^{-1} = G_{loc}^{-1}(i\omega_n) + \Sigma(i\omega_n) \, . \quad (3.4)$$

3. To get the impurity Green function we perform two averaging processes; namely the averaging over local spin orientations and over impurity configurations. For a nonmagnetic impurity site, the impurity Green function is simply equal to the mean-field: $\hat{G}_{non} = \mathcal{G}$. On the other hand, the impurity Green function of a magnetic site is given by $\hat{G}_{mag}(i\omega_n) = [\mathcal{G}^{-1}(i\omega_n) + J_H \mathbf{S} \cdot \boldsymbol{\sigma}]^{-1}$. This magnetic impurity Green function is then averaged over the local spin orientations weighted by the angular distribution function:

$$P(\hat{\mathbf{S}}) = \frac{\exp\left(-\tilde{S}_{eff}(\mathbf{S})\right)}{\mathcal{Z}} \, ; \mathcal{Z} = \int d\Omega_{\hat{\mathbf{S}}} \, \exp\left(-\tilde{S}_{eff}(\mathbf{S})\right) \, . \quad (3.5)$$

Here,

$$\tilde{S}_{eff}(\mathbf{S}) = -\log\det\left[\frac{1}{i\omega_n}\left(\mathcal{G}^{-1}(i\omega_n) + J_H\mathbf{S}\cdot\boldsymbol{\sigma}\right)\right]e^{i\omega_n 0^+} \ . \tag{3.6}$$

The extra factor of $\frac{1}{i\omega_n}$ is for numerical convergence. Thus,

$$\langle\hat{G}_{mag}(i\omega_n)\rangle_{\hat{\mathbf{S}}} = \int d\Omega_{\hat{\mathbf{S}}} P(\hat{\mathbf{S}})\left[\mathcal{G}^{-1}(i\omega_n) + J_H\mathbf{S}\cdot\boldsymbol{\sigma}\right]^{-1} \ . \tag{3.7}$$

The total impurity Green function is obtained through the configurational averaging:

$$G_{imp}(i\omega_n) = x\langle\hat{G}_{mag}(i\omega_n)\rangle_{\hat{\mathbf{S}}} + (1-x)\mathcal{G}(i\omega_n) \ , \tag{3.8}$$

where x denotes the impurity concentration.

4. To close the algorithm loop we calculate the new self-energy through Dyson's equation again:

$$\Sigma(i\omega_n) = \mathcal{G}(i\omega_n)^{-1} - G^{-1}_{imp}(i\omega_n) \ . \tag{3.9}$$

The steps are repeated again starting from (3.3) until the self-consistency is reached, i.e. when $G_{loc} = G_{imp}$.

3.3 Typical Medium Theory

In a disordered system, it could happen that the disorder potential is strong enough to trigger a metal-insulator transition (MIT), Anderson localization transition, as described originally by Anderson [91]. A study by Richardella *et al.*[58] shows that this disorder-driven metal-insulator transition may play an important role in determining the magnetic mechanism of (Ga,Mn)As. Therefore, it is important to understand how the Anderson localization takes place in DMS. Unfortunately, it is not easy to show theoretically how a system goes toward the Anderson localization transition because it is not so clear what should be an appropriate order parameter for the Anderson localization. Localization is

a phenomenon manifested in transport properties, which are two-particle Green functions, whereas regular mean-field methods only consider quantities that are related directly to the one-particle Green function.

In 2003 Dobrosavljević *et al.*[92] introduced a *new* mean-field approach called the typical-medium theory that proposes the typical density of states (TDOS) as the appropriate order parameter for the Anderson localization. They argued that TDOS describes the typical escape rate of particles in a disordered system, and thus is directly related to the conductivity. Furthermore, they also discuss that TDOS can be well represented by the geometrical average of the local density of states:

$$\rho_{typ}(\omega) = \exp\left\{\int d\varepsilon_i P(\varepsilon_i) \log \rho(\omega, \varepsilon_i)\right\} \ , \tag{3.10}$$

where ε_i is a parameter describing the random potential whereas $P(\varepsilon_i)$ is the probability density (weight) of an impurity site with the potential value ε_i. TMT can be incorporated directly within DMFT due to the formulation of TMT that was following DMFT reasoning [92].

Chapter 4
Mn Valence State and Low-Energy Models

As described previously in Chapter 1, Mn valence state has considered important in the study of the $Ga_{1-x}Mn_xN$ DMS. Despite its widely accepted importance, the Mn valence state in $Ga_{1-x}Mn_xN$ is still controversial. Early experimental [93, 94, 95] and density functional theory (DFT) studies [96, 97, 98, 99, 100, 101] demonstrated a partially filled impurity band formed deeply in the band gap with a significant Mn d character, suggesting a Mn^{3+} (d^4) configuration different from the Mn^{2+} (d^5) one in $Ga_{1-x}Mn_xAs$ [102]. Later, both x-ray absorption spectroscopy (XAS) studies [103, 104, 105] and optical absorption analysis [106, 107] also concluded a Mn valence state of 3+ (d^4). However, other XAS studies [108, 109, 110] demonstrate that Mn is predominantly Mn^{2+} (d^5). A similar conclusion was also reached by electron spin resonance [39] and magnetic measurements [40]. Clearly, a resolution of the uncertainty about the Mn valence state is imperative for further progress in the understanding and engineering of the $Ga_{1-x}Mn_xN$ DMS.

In this Chapter, we report our investigation on the controversial Mn valence state in $Ga_{1-x}Mn_xN$. Our first-principles Wannier-functions based analysis [82] covering the high-energy Hilbert space demonstrates unambiguously that the Mn valence is close to 2+ (d^5) but with a mixed spin configuration that gives average magnetic moments of $4\mu_B$ (*not* $5\mu_B$). Interestingly, at the more relevant lower-energy scale, due to the proximity of N s and p energy levels to the Mn d level, the dual nature of the doped hole can be realized. Defining Wannier orbitals (WOs) in a narrower energy range, we show the feasibility of both the effective d^4 and d^5 descriptions, which are convenient to describe different physical aspects of $Ga_{1-x}Mn_xN$. The resulting effective d^4 picture offers the simplest description of the local magnetic moment and the Jahn-Teller distortion while the effective d^5 picture is most suitable for long-range magnetic order. Moreover, our first-principles result reveals

several strong physical effects absent in previous studies. Our study not only resolves one of the outstanding key puzzles in the field of DMSs, but also highlights the generic need for multiple effective descriptions in describing the rich low-energy physics in interacting systems in general.

4.1 Method

We start by performing first-principles DFT calculations in a zinc blende supercell of 64 atoms ($Ga_{31}MnN_{32}$) (Figure 4.1) within the full-potential linearized augmented-plane-wave method [76]. The lattice parameter we used here is from the previous study [111], that is $a = 4.542$ A for GaN and thus for $Ga_{31}MnN_{32}$ the lattice constant is $2a = 9.084$ A. We

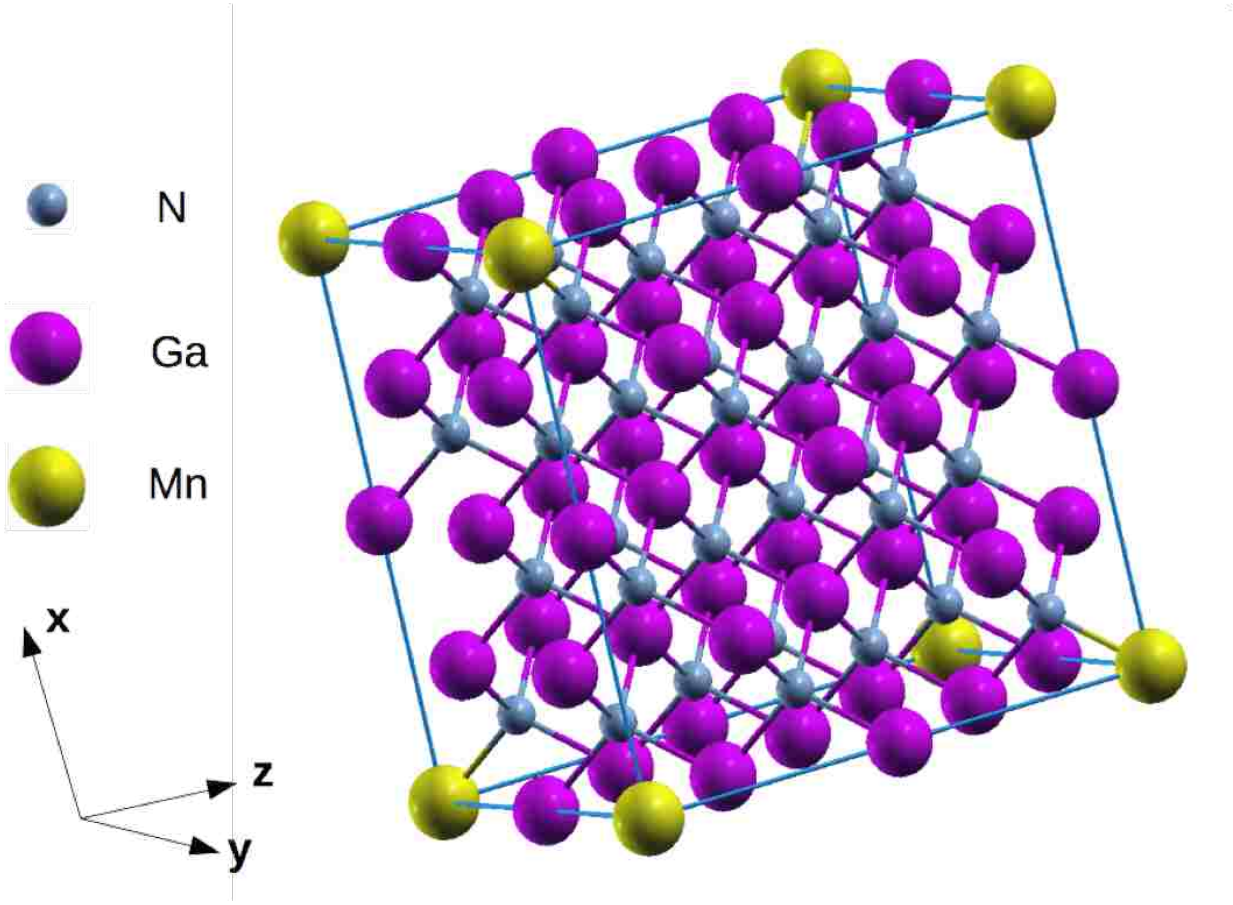

Figure 4.1: The supercell structure of $Ga_{31}MnN_{32}$ with the lattice length is $2a = 9.084$ A, where a is the lattice constant of GaN.

did not do structural optimization in our calculations since a study by B. Sanyal et al. [97] shows that the atomic relaxation changes the bond length between Mn and N very little. Furthermore, from comparing previous DFT studies of $Ga_{1-x}Mn_xN$ [96, 97, 98, 111, 101] that used different lattice parameters we also observe that the variation in the lattice parameters barely affects the result.

We apply the LDA+U approximation [72] to Mn atoms with $U = 4$ eV and $J = 0.8$ eV. These parameters U and J are chosen based on previous studies of $Ga_{1-x}Mn_xN$ with LDA+U [97, 98]. These studies emphasize the importance of the use of LDA+U to appropriately treat Mn d orbitals that are quite localized. Furthermore, in Reference [97], it is discussed that although the inclusion of U and J are important, the exact values of U and J do not really matter since it is shown further in their paper that their result did not change much as they varied U from 4 to 7 eV.

We then construct WOs with the downfolding method described [82] in three different ways to effectively integrate out various degrees of freedoms, to analyze the electronic structure at different energy scales, and to illustrate the relevant physical effects. As will become clear below, the use of WOs is crucial in the analysis, for example in counting the charges.

4.2 Results and Discussion

First, to address the question on the valence state of Mn we look into the high-energy properties by analyzing the resulting density of states with N-sp^3, Ga-sp^3, and Mn-d symmetries covering the energy range of $[-18.0, 9.0]$ eV. Figure 4.2(a) shows partially filled impurity bands lying deep in the band gap similar to previous DFT analyses [96, 97, 98, 99, 100, 48]. Particularly, Figure 4.2 (b) shows that the Mn-t_{2g} impurity levels are strongly hybridized with the surrounding N-sp^3 orbitals, such that the total weight in the N orbital slightly exceeds that of the Mn. Integrating the DOS up to the Fermi energy, we find the Mn occupation to be 5.0, corresponding to the Mn valence of 2+ (d^5). This result is quite different

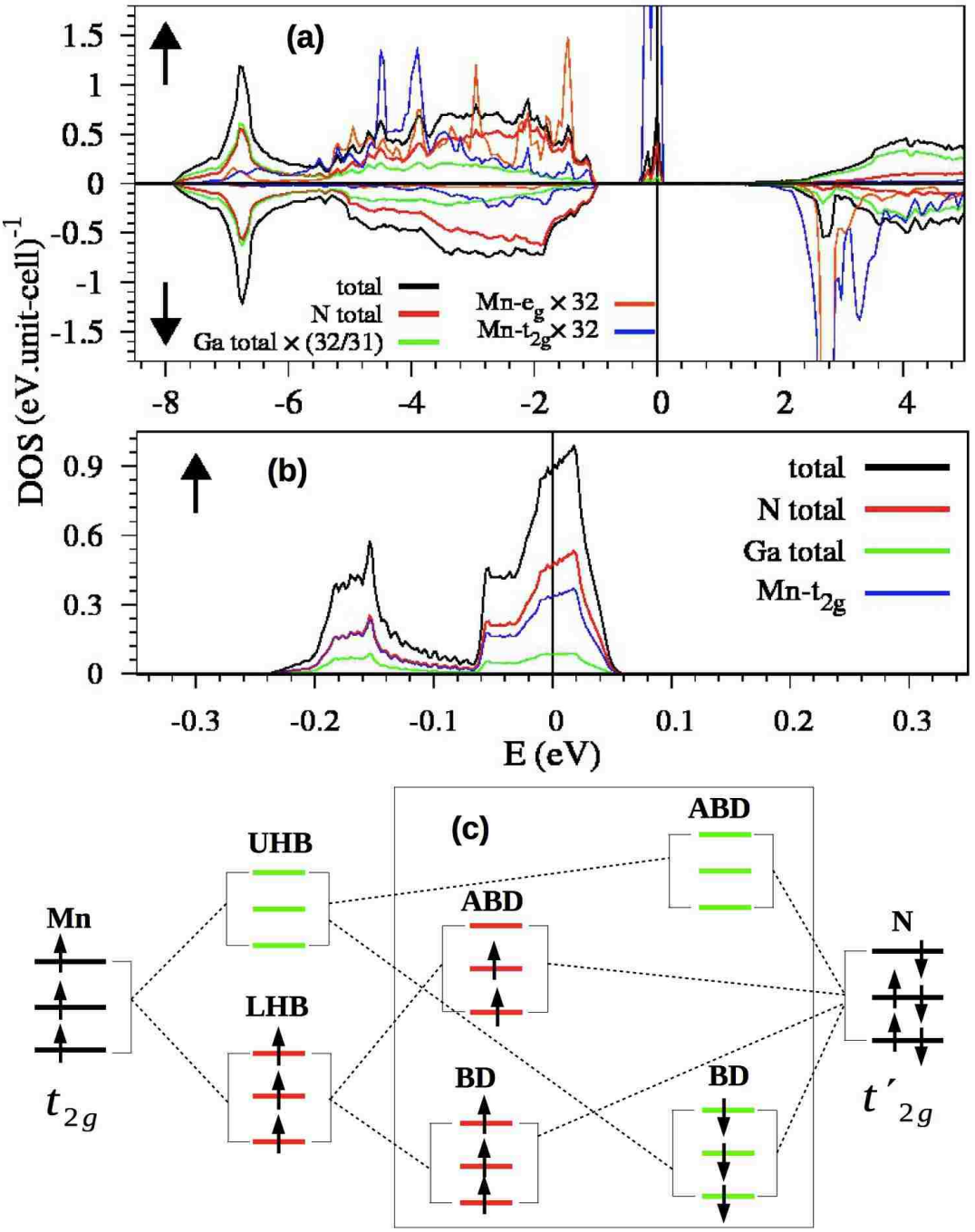

Figure 4.2: (a) Total and partial densities of states (DOSs) of $Ga_{31}MnN_{32}$ with the Fermi energy (E_F) at 0 eV. The partial DOSs have been scaled up in units of "per atom of this kind." (b) The DOS of the impurity bands around E_F in units of "per GaN primitive unitcell". (c) Illustration of the hybridization of Mn-N orbitals. Up and down arrows represent spin majority and minority, respectively. UHB (LHB) denotes upper (lower) Hubbard bands, whereas BD (ABD) denotes bonding (antibonding). Note that two electrons residing in the spin-majority e_g orbitals are not shown here.

from the value of 4.59 presented in a previous DFT study [96], but the distinction is easily understandable from the fact that counting charges within an artificially chosen muffin tin around the Mn ion would necessarily miss the interstitial contributions. Our WOs, on the other hand, span the entire Hilbert space up to 9 eV and leave no unaccountable charges.

However, this seemingly clean Mn^{2+} charge distribution contributes to a total spin of only 4.0 μ_B (*not* 5 μ_B). Therefore, it should not (and cannot) be understood simply from the pure ionic d^5 configuration. Indeed, Figure 4.2(a) shows clearly that part of the 5.0 d electrons resides in the spin minority channel spreading over a large energy range, as a consequence of the strong hybridization with the N orbitals. A simpler visualization of this beyond-ionic configuration is given by Figure 4.2(c) that summarizes the basic building blocks of the electronic structure. It is now clear that the Mn ion hosts part of a hole in the antibonding orbitals of the lower Hubbard bands (LHBs), and part of three electrons in the bonding orbitals of the upper Hubbard bands (UHBs). Specifically, we found 0.5 electrons in the Mn spin-minority channel, and 4.5 in the majority one, giving a net moment of 4.0 μ_B. (The N orbitals that hybridize with Mn orbitals, named N-t'_{2g} in Figure 4.2(c), will be defined in detail below.)

Obviously now, the strong hybridization between Mn and N orbitals renders the high-energy ionic picture based on atomic orbitals completely inapplicable in the lower-energy sector, in which the renormalized orbitals absorb the hybridization upon integrating-out the higher-energy degrees of freedom. In other words, at low energy, electrons are no longer able to reside in Mn or N atomic orbitals, but only in Mn-N hybrids. Therefore, debating the ionic valency with atomic orbitals is of no physical significance for the low-energy behavior of the system. Instead, the physics should be described by effective or "renormalized" Mn and N orbitals.

Interestingly, the proximity of the N and Mn orbital energies, which enhances the hybridization and other quantum effects, also enables the generic possibility of multiple representations of the many-body system. It is feasible to derive multiple low-energy effec-

tive pictures, depending on which is more convenient for describing the physical properties of interest. Below, we demonstrate this fundamental feature by constructing various low-energy effective WOs that correspond to integrating-out higher-energy degrees of freedom differently. Specifically, we show that both effective d^4 and d^5 pictures can be derived, and both are useful for describing certain properties.

We start with the local properties of $Ga_{1-x}Mn_xN$. Figure 4.2(b) shows a $\frac{2}{3}$–filled impurity level, corresponding to two electrons residing in three degenerate "effective" t_{2g} WOs. One thus expects a strong local Jahn-Teller instability toward splitting the degeneracy into $2+1$. Indeed, the Jahn-Teller instability has been found in previous studies [111, 112]. It is easier to describe this local physics using an "effective" d^4 picture. Figure 4.3 (a) shows one of the effective $\widetilde{\text{Mn}}$-t_{2g} WOs corresponding to the impurity levels between $[-0.4, 0.4]$. It has the symmetry of the Mn-t_{2g} orbital, but with large tails in the surrounding N ions, incorporating the antibonding hybridization illustrated in Figure 4.2(c). It is in this effective $\widetilde{\text{Mn}}$-t_{2g} WOs that an effective d^4 picture is realized: A threefold degenerate WO hosting two electrons, which then split into $2+1$ orbitals upon orbital polarization. (The other two electrons reside in the spin-majority effective e_g WOs.) This effective d^4 picture also gives a local moment of $4\mu_B$ that is really the one fluctuating at low energy, with a form factor [86, 113] extending to neighboring N ions in real space.

An interesting point that emerges here is that the hybridization with Mn-t_{2g} naturally splits the surrounding four N-sp^3 orbitals, one from each N ion pointing toward Mn, into a set of $3+1$ configurations. The threefold degenerate ones have the correct signs to match each of the Mn-t_{2g} orbitals: $(+,+,-,-)$, $(+,-,+,-)$, $(+,-,-,+)$, while the fourth one with sign $(+,+,+,+)$ does not couple to the Mn-t_{2g} orbitals. One thus can conveniently name them N-t'_{2g} and N-s' WOs centered at the Mn site. The four tails of the WOs in Figure 4.3 (a) give an example of one of these N-t'_{2g} orbitals which in Figure 4.2(c) hybridize with Mn-t_{2g}. These N-t'_{2g} are the ones being integrated out to derive the effective d^4 picture. Note that this change of perspective is the same as that employed in the construction of the

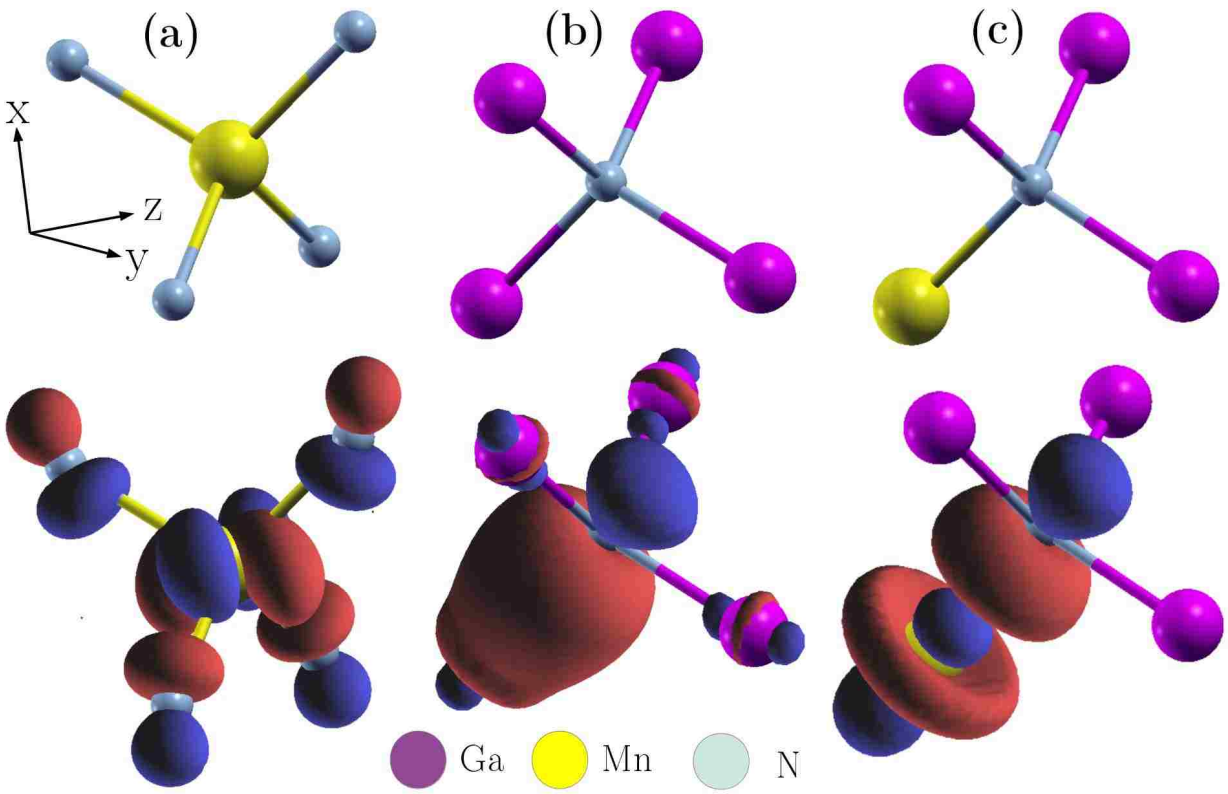

Figure 4.3: Illustration of the WOs used in (a) low-energy effective d^4 and (b), (c) the effective d^5 picture. The upper panels show the local crystal structure, while the lower panels plot the isosurface of (a) $\widetilde{\text{Mn}} - t_{2g}$, and (b)(c) $\widetilde{\text{N}} - sp^3$ WOs at 0.07 bohr$^{-3/2}$.

well-known Zhang-Rice singlet in the cuprate high-temperature superconductors [114, 115], and the same concept has been applied to the study of local excitations in correlated NiO [113, 116] and LiF [117, 118].

The above effective d^4 picture, while ideal to study the Jahn-Teller instability and other local properties like the local magnetic moment and local excitations, is not suitable for studying long-range properties. This is because the wave nature of the GaN orbitals, after being integrated out, generates effective magnetic couplings that are impurity-configuration dependent between the $\widetilde{\text{Mn}}$ WOs at different sites. For instance, the magnetic coupling does not only depend on the distance between pairs of Mn impurities [48], but also on the position of other nearby Mn impurities, corresponding to three-body and four-body interactions [119].

Therefore, we proceed to derive an effective d^5 picture suitable for studying long-range properties, by integrating out charge fluctuation involving Mn-d and Ga orbitals in the multiorbital Anderson Hamiltonian, leaving only the doped hole in the antibonding WOs with primarily N-sp^3 character. From this we obtain a spin-fermion Hamiltonian with a few novel physical effects: $H_{\text{eff}} = H_0 + \Delta$, where

$$H_0 = \sum_{\mathbf{i}\mathbf{i}'mm'\sigma} t_{\mathbf{i}\mathbf{i}'}^{mm'} c_{\mathbf{i}m\sigma}^{\dagger} c_{\mathbf{i}'m'\sigma} + \ H.c. \tag{4.1}$$

is the Hamiltonian of pure GaN, and

$$\begin{aligned} \Delta = & \sum_{\mathbf{j}\mathbf{i}\mathbf{i}'mm'\sigma} T_{\mathbf{j}\mathbf{i}\mathbf{i}'}^{mm'} c_{\mathbf{i}m\sigma}^{\dagger} c_{\mathbf{i}'m'\sigma} \\ & + \sum_{\substack{\mathbf{j}\mathbf{i}\mathbf{i}'mm' \\ \sigma\sigma'}} J_{\mathbf{j}\mathbf{i}\mathbf{i}'}^{mm'} c_{\mathbf{i}m\sigma}^{\dagger} \boldsymbol{\tau}_{\sigma\sigma'} c_{\mathbf{i}'m'\sigma'} \cdot \hat{\boldsymbol{S}}_{\mathbf{j}} \ + \ H.c. \end{aligned} \tag{4.2}$$

contains the influence of the (Ga,Mn) substitution at the primitive unit cell $\mathbf{j}$, and is thus referred to as the impurity potential. As usual, $c_{\mathbf{i}m\sigma}$ ($c_{\mathbf{i}m\sigma}^{\dagger}$) annihilates (creates) an electron with spin σ at unit cell $\mathbf{i}$ in the mth WOs. $t_{\mathbf{i}\mathbf{i}'}^{mm'}$ contains the orbital energy (when $\mathbf{i} = \mathbf{i}'$ and $m = m'$) and hopping integral of the effective $\widetilde{\text{N}}$-sp^3 WOs. $T_{\mathbf{j}\mathbf{i}\mathbf{i}'}^{mm'}$ and $J_{\mathbf{j}\mathbf{i}\mathbf{i}'}^{mm'}$ represent spin-independent and spin-dependent impurity potentials, respectively. $\hat{\boldsymbol{S}}_{\mathbf{j}}$ and $\boldsymbol{\tau}_{\sigma\sigma'}$ are the spin-$\frac{5}{2}$ unit vector and elements of the Pauli's matrices, respectively, and $H.c.$ denotes the Hermitian conjugate. To get a better understanding of the origin of this generalized spin-fermion model we illustrate the derivation of the impurity potentials from perturbation theory using a simple model in Appendix A.

Note that the four WOs with the same unit-cell index are defined to be the $\widetilde{\text{N}}$-sp^3 WOs pointing toward the central Ga/Mn ion, one from each surrounding N ion. With the help of symmetry considerations (see Appendix A) we choose the proper WOs' subspace corresponding to integrating out the Mn and Ga orbitals. These WOs can be constructed from our DFT results within the energy range $[-18.0,\ 0.4]$ eV, as shown in Figure 4.3 (b)

and 4.3 (c). In their hybridization tails, one observes clearly bonding with Ga-sp^3 [Figure 4.3(b)] and antibonding with Mn-d [Figure 4.3(c)].

Having these WOs at hand, we can then represent the relevant part of the DFT self-consistent Hamiltonian and collect its term into the form of Eqs. (4.1) and (4.2). Since this is a faithful representation of the relevant components of the DFT Hamiltonian, its validity is actually beyond the second order in the atomic hopping integral. A few leading parameters in our results are given in Table 4.1. As expected, they show a rapid decay with the distance from the impurity site.

Table 4.1: Leading parameters in the impurity potential in meV near the impurity site $\mathbf{j}$ ($m \neq m'$). NN($\mathbf{j}$) and NNN($\mathbf{j}$) denote nearest and next nearest neighboring sites.

	$T^{mm}_{\mathbf{jji'}}$	$T^{mm'}_{\mathbf{jji'}}$	$J^{mm}_{\mathbf{jji'}}$	$J^{mm'}_{\mathbf{jji'}}$
$\mathbf{i'} = \mathbf{j}$	2488	-170	1752	-633
$\mathbf{i'} = \mathrm{NN}(\mathbf{j})$	406	885	449	800
$\mathbf{i'} = \mathrm{NNN}(\mathbf{j})$	15	68	< 10	38

Interestingly, our results reveal a few new physical effects on the carriers besides the previously proposed [49] antiferromagnetic exchange with the local moment ($J^{mm}_{\mathbf{jjj}} = 1752$ meV in Tabel 4.1). First, the impurity potential contains a strong shift of the orbital energy ($T^{mm}_{\mathbf{jjj}} = 2488$ meV), even *stronger* than the exchange above. This reflects the distinct atomic orbitals of Mn (the impurity) and Ga (the host) being integrated out. In fact, our test shows that if one were to ignore just this parameter, the impurity level [red bands in Figure 4.4(a)] would have dropped outside the band gap [c.f. Figure 4.4(b)], totally destroying the physical characteristics of the system. Physically, this large orbital energy shift of course induces a strong impurity scattering and a strong tendency toward Anderson localization [91], affecting the carrier mobility, the activation energy, and almost every other essential physical aspect of a semiconductor, in addition to altering the effective magnetic coupling between Mn ions. Second, our results also show a strong exchange-assisted hopping ($J^{m\neq m'}_{\mathbf{jji'}} = -633$ meV and 800 meV in Tabel 4.1 close to the impurity site.) Again,

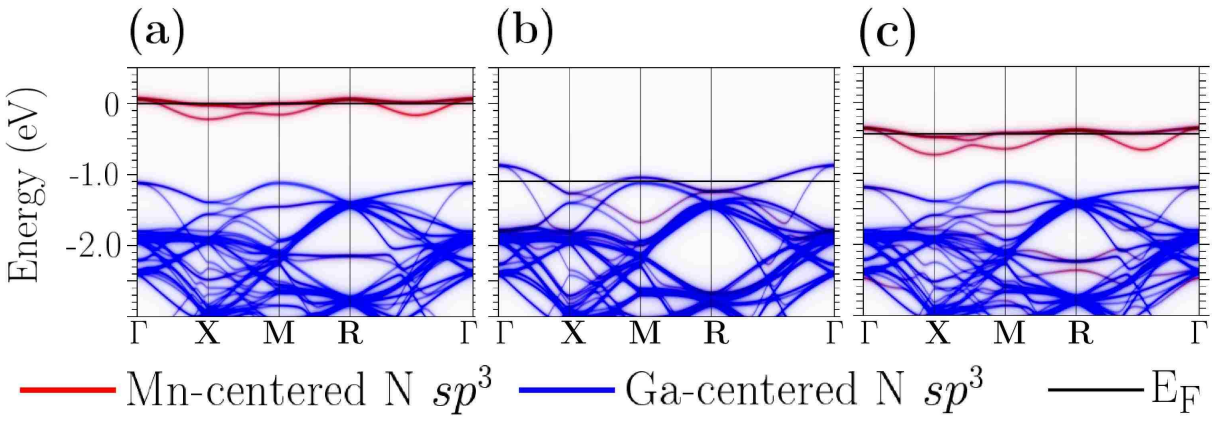

Figure 4.4: The spin-majority band structure of $Ga_{31}MnN_{32}$ (a) with complete parameters, (b) with the leading orbital energy shift $T^{mm}_{\mathbf{jjj}} = 2488$ meV removed, and (c) with the two leading exchange-assisted parameters $J^{mm'\neq m}_{\mathbf{jjj}} = -633$ and $J^{mm'\neq m}_{\mathbf{jji'}} = 800$ meV with $\mathbf{i'} = \mathrm{NN}(\mathbf{j})$ removed.

Figure 4.4(c) shows that ignoring these two terms leads to a much smaller spin-dependent splitting of the impurity level. Therefore, they not only add to the above impurity effects but also directly modify the magnetic exchange and ordering of Mn impurities. Both of these two effects are very strong and comparable in strength to the exchange effect included in previous studies, and thus will need to be further investigated in the future.

It is useful to remark that our approach of employing multiple pictures in understanding different low-energy properties of a many-body system have been used in other strongly correlated materials, for example, in the manganites and the cuprates. Specifically for the cuprates, the Zhang-Rice singlet description [114] and Emery-Reiter three-spin polaron description [120] are exactly effective d^8 and d^9 pictures, parallel to our d^4 and d^5. The d^8 approach integrates the oxygen degrees of freedom out, resulting in a reduced local magnetic moment $S = 0$, similar to our effective d^4 picture that absorbs implicitly the GaN orbitals and has a smaller moment $S = 2$. On the other hand, the d^9 picture integrates the charge fluctuation involving the Cu orbitals out and results on doped holes propagating in O orbitals that are correlated antiferromagnetically with the surrounding Cu $S = 1/2$ spins, similar to our effective d^5 picture in which carriers live in effective $\widetilde{\mathrm{N}}$-sp^3 WOs that correlated antiferromagnetically with the Mn $S = 5/2$ spins. Naturally, the more complete

d^9 picture of cuprates and our d^5 picture of (Ga,Mn)N cover a larger energy range than the d^8 and d^4 pictures, respectively, and thus allow richer physical behaviors in general.

4.3 Summary

To summarize, by investigating the current debate on the Mn valence in $Ga_{1-x}Mn_xN$, we advocate three general points in correlated materials: 1) atomic or ionic valence is only meaningful for high-energy properties but is not very relevant to the low-energy physical properties; 2) it is often possible to derive multiple effective pictures by integrating out the less relevant degrees of freedom; and 3) for challenging correlated systems, one thus should take advantage of such flexibility and employ the most convenient picture for describing the physical properties of interest. Specifically, we found the Mn valence of 2+, but with a nonatomic spin of $4\mu_B$, illustrating the inadequacy of ionic valence in an atomic picture. We then demonstrate the feasibility of an effective d^4 picture (naturally with $S = 4\mu_B$) suitable for studying local instabilities and excitations. In addition, we derive an effective d^5 approach that can be used for future studies of long-range magnetic order, nonlocal magnetic correlation, and other transport properties. Particularly, our d^5 model demonstrates a few novel physical effects beyond previous considerations in the field. Our results clarify the intrinsic dual nature of the doped holes in the DMS and pave the way for future realistic studies of the magnetism in these systems. Our study not only resolves one of the outstanding key puzzles in the field, but also emphasizes the general need for multiple effective pictures to describe the rich low-energy physics in many-body systems in general.

Chapter 5
Disorder-Driven Localization in Diluted Magnetic Semiconductors

5.1 Introduction

Until relatively recently, the mean-field Zener model of Dietl was the accepted paradigm for diluted magnetic semiconductors (DMS) systems [28, 33]. Here, a magnetic exchange between localized Mn moments mediated by the valence band (VB) holes drives the magnetism. This mechanism is also known as the valence-band (VB) model. However, recent experiments have now led to wide acceptance that the VB is nearly nonmagnetic and does not overlap with the impurity band (IB) [121]. This gave rise to another model known as the impurity-band (IB) model. This model, furthermore, is supported by evidence that the magnetic properties of DMS are determined by the location of the chemical potential in this distinct IB brought on by Mn doping, and even by the Anderson localization of the IB carriers [122, 123, 124]. At the model level, however, some previous important studies [125, 126] have reported a possible IB-VB crossover resulting from adjusting parameters such as impurity and hole concentrations.

Despite the success on describing the transition of the carrier from IB-like to VB-like, model-level studies did not describe the Anderson's localization scenario that might happen in real materials. A direct probe of the IB states in (Ga,Mn)As by local tunneling shows that the local density of states follows a log-normal distribution at the verge of the localization transition [58] and the typical value of the distribution is vanishing. The fact that DMS can undergo an Anderson localization transition makes DMS more challenging, especially if we consider the competition between localization and magnetism in (Ga,Mn)As which is still not well understood [123, 124].

In this Chapter, we report our investigation of the Anderson localization transition in DMS using a spin-fermion model within the typical medium theory (TMT) framework. Using the typical density of states (TDOS) as an order parameter we find that the TDOS vanishes below a critical doping concentration, indicating an Anderson localization transition. Furthermore, our findings demonstrate TMT as a powerful means to study the Anderson localization in DMS.

5.2 Method

We use an extended spin-fermion Hamiltonian as described in Chapter 3:

$$H = -t \sum_{ij\sigma} c^{\dagger}_{i\sigma} c_{j\sigma} + V \sum_{p} n_p - J \sum_{p} m_p S \ . \tag{5.1}$$

Here we only use a simple kinetic energy term where i and j represent all sites and their first-nearest neighbors, whereas the random potentials are the spin-independent (V) and spin-dependent (J) potentials where p represents impurity sites. $n_p = n_{p\uparrow} + n_{p\downarrow}$ and $m_p = n_{p\uparrow} - n_{p\downarrow}$, respectively, are the carrier density and polarization. Strictly speaking, this is just a binary alloy model with different potentials for the up and down spins. The non-magnetic potential, V, is added to incorporate a more realistic situation where the presence of V in some materials is comparable to J, and thus plays an important role in determining the VB-IB crossover [125, 126]. Our goal with this model is to study how ferromagnetism competes with the Anderson's localization in DMS.

In order to solve the Hamiltonian, we employ TMT as described in Section 3.3. TMT is an extension of the coherent potential approximation (CPA) [127] in which the disordered lattice is replaced by an impurity placed in an arithmetically averaged momentum-independent effective medium. While the CPA has been successful in describing some one-particle properties, such as the density of states (DOS) in disordered alloys [127], it fails to describe the Anderson localization transition. This failure stems from the arithmetic

average used to define the effective medium, which always favors the metallic state. In the TMT, the arithmetic average DOS is replaced by the geometric average, or typical, DOS [92, 128, 129] $\rho_{typ} = \exp\langle \ln \rho \rangle$, which vanishes at the localization transition. The impurity Green function is calculated from the Hilbert transform of ρ_{typ}: $G(\omega') = \int d\omega \frac{\rho_{typ}(\omega)}{\omega' - \omega}$, and the host Green function is given by $\mathcal{G}^{-1} = G^{-1} + \Sigma$, where Σ is the impurity self-energy.

Within the TMT, the ferromagnetic phase exists at zero temperature as long as the effective polarization of the host Green function

$$\mathrm{m_{eff}} = |\langle n_{i,\uparrow} - n_{i,\downarrow} \rangle| = \left| -\sum_{\sigma} \sigma \int_{\mathrm{E_F}}^{\infty} \frac{d\omega}{\pi} \mathcal{G}''_{\sigma}(\omega) \right| \tag{5.2}$$

remains finite. Here,

$$\mathcal{G}''_{\sigma} = \frac{\Gamma''_{\sigma}(\omega)}{(\omega - \Gamma'_{\sigma}(w))^2 + \Gamma''_{\sigma}(\omega)^2} \ . \tag{5.3}$$

Despite the simplicity of this model, it can illustrate the competition between ferromagnetism and localization. The imaginary part of the host Green function, $\mathcal{G}''_{\sigma}$, is proportional to the imaginary part of the hybridization, Γ''_{σ}, between the impurity site and the host, and Γ''_{σ} goes to zero at the Anderson localization transition [92]. This means that the polarization vanishes when $\Gamma''_{\sigma}(\omega) = 0$ for $\omega > \mathrm{E_F}$ where $\mathrm{E_F}$ is the Fermi level. Thus, even this simple model of DMS can describe the competition between magnetization and localization.

5.3 Results and Discussion

Fig. 5.1 shows the average density of states (ADOS) calculated from CPA and hybridization (Γ) from TMT for up ($\uparrow$) and down ($\downarrow$) spins at the ferromagnetic phase. Here, the parameters we use are $J = 0.85$, $V = 0.15$ and percentage of dopants $x = 0.100$. As can be seen, for these parameters, the IB only develops at one particular spin configuration, namely, the spin down configuration. This is because the non-magnetic potential suppresses the development of the IB at the spin up configuration. It is worth mentioning that at this

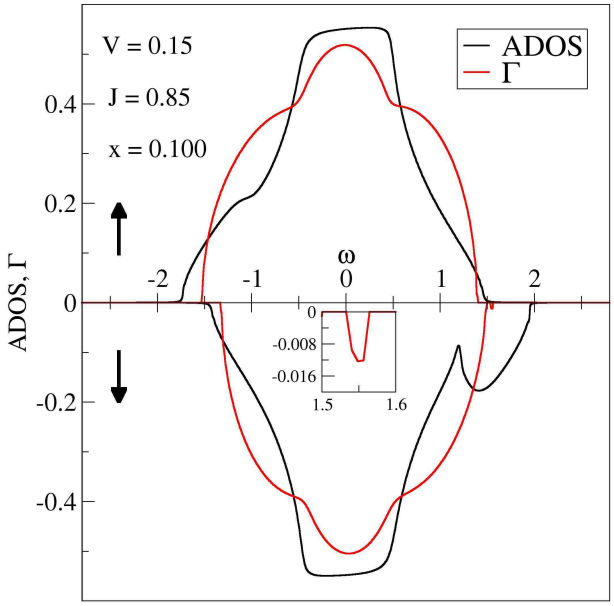

Figure 5.1: Average density of state (ADOS) and hybridization (Γ) plots for the following parameters $V = 0.15$, $J = 0.85$, and $x_c = 0.100$. The inset shows the zoomed-in impurity-band (IB) hybridization (Γ).

point due to an imbalance between the up and down densities of states, the system could always have a ferromagnetic phase by adjusting the hole filling or the Fermi level to be at the IB, although the transport properties of the system might change as it goes from the IB to VB regimes. We also note that at these particular parameters the ADOS displays the IB-VB crossover, while the hybridization from TMT (zoomed in the inset) indicates that the system is still in the IB regime. Furthermore, in Fig. 5.2a (zoomed-in on the right side) we see that Γ evolves rapidly as the doping concentration increases, whereas ADOS barely changes. Finally, we find that Γ undergoes the IB-VB crossover at $x = 0.117$. From this, we can say that although TMT and CPA can produce the IB-VB crossover, the TMT estimates a higher doping for the IB-VB crossover to occur.

Next, as seen in Figure 5.2b (zoomed-in on the right side) Γ shrinks as we lower the doping concentration and disappears below $x = 0.093$. Meanwhile, ADOS again barely changes. The disappearance of Γ at IB indicates that the system undergoes Anderson's localization transition. As the hybridization disappears, the ferromagnetic phase is sup-

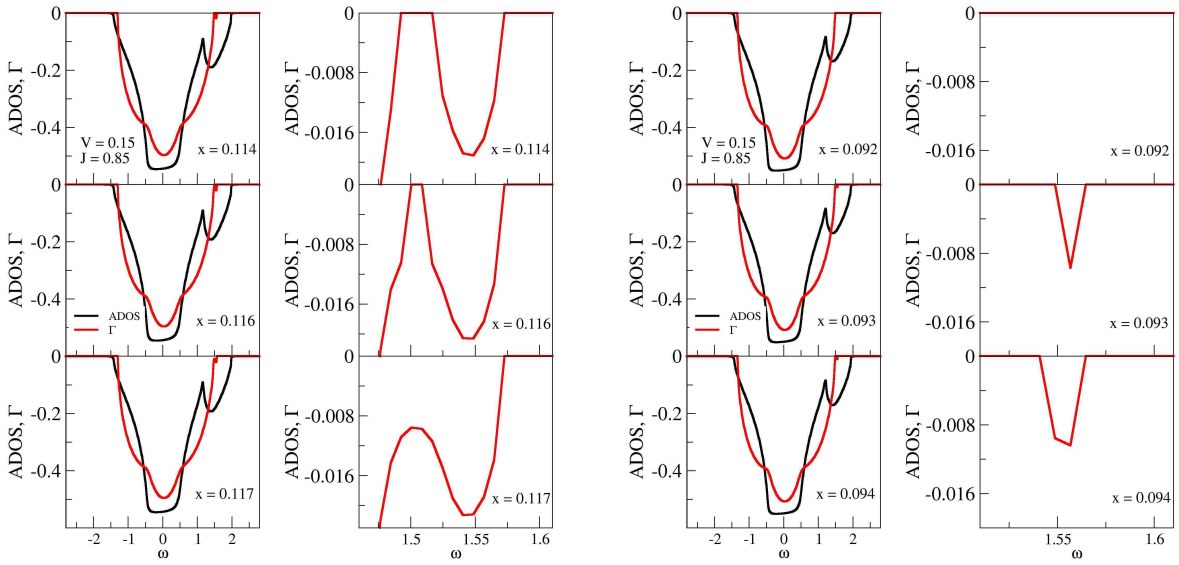

Figure 5.2: Average density of state (ADOS) and hybridization (Γ) of the down spin for the same V and J parameters as Figure 5.1 but different values of doping, x. The left sides show their normal size, whereas the right sides show the zoomed-in version around the impurity band (IB). (a) The IB-VB crossover transition as we increase x. (b) The Anderson transition as we change x from low to high value.

pressed since the carriers get trapped and are not able to mediate the interactions between local spins to form long-range ferromagnetic order.

We can more clearly see this suppression in Fig. 5.3 which shows the effective polarization (dots) of the IB as a function of the doping (the red line is used as a guide to the eyes.) The polarization linearly decreases as the doping decreases. Note, however, that the critical concentration for the insulator-ferromagnetic metal transition is strongly overestimated when compared with experimental values, as expected from a mean field method.

5.4 Conclusion

To summarize, we have investigated the Anderson localization in DMS systems with a simple spin-fermion model which was then solved using TMT. We observed the IB-VB crossover in DMS as found in previous studies [125, 126]. Furthermore, by looking at the evolution of the hybridization, we also observed the metal-insulator Anderson transi-

tion which was never previously shown in any theoretical DMS studies. This demonstrates the power of TMT to reveal Anderson localization in DMS even within only a simple model.

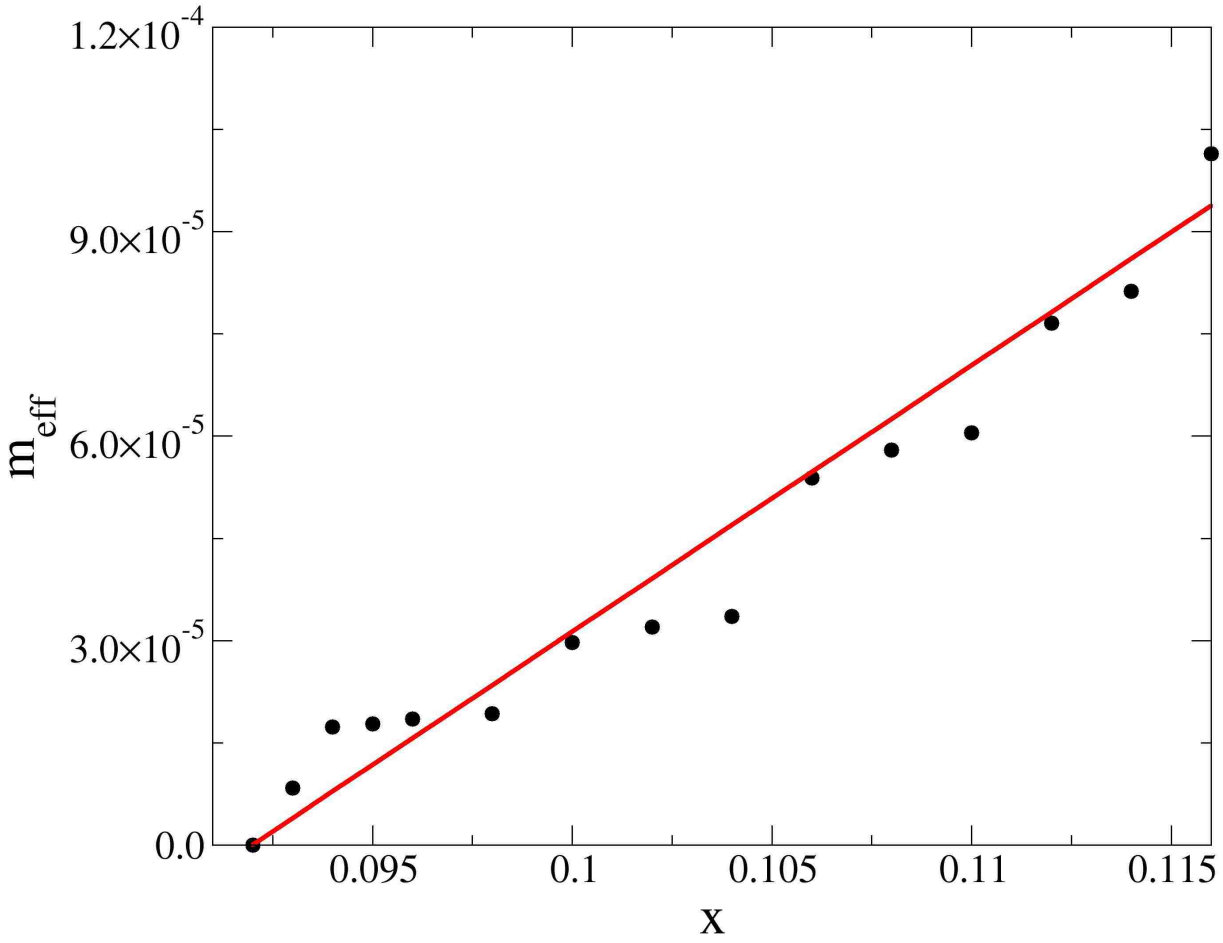

Figure 5.3: The polarization (m_{eff}) as a function of the doping concentration (x) (red line is a guide to the eyes.)

Chapter 6
First-Principles study of Ta_2PdSe_6

6.1 Introduction

Magnetoresistance is a phenomenon where the resistivity of a material changes when exposed to an external magnetic field. This phenomenon was first discovered in nickel and iron by W. Thomson in 1856 [59] when he was studying the effect of a magnetic field on metals. Since then we know that magnetoresistance occurs naturally in many metals. Furthermore, the mechanism behind magnetoresistance is not unique. There are several mechanisms that can cause magnetoresistance in materials. In many normal metals, magnetoresistance is caused by the existence of different charge carrier types with each having a different density and/or effective mass and/or scattering rate. The presence of a magnetic field will affect each carrier type differently through the Lorentz force causing compensation to the net current, and thus changing the apparent resistivity. Some other mechanisms are current transfer through multi-layers materials as in giant magnetoresistance devices [1] and double-exchange mechanism [60].

Recently, Liu and Mao [61] measured magnetoresistance on a sample of Ta_2PdSe_6. Figures 6.1a & b show their experimental results [61]. In Figure 6.1a, the resistivity is plotted as a function of temperature for different applied magnetic fields. As can be seen, below certain temperatures the resistivities behave differently for different applied fields, i.e. clear evidence of magnetoresistance in Ta_2PdSe_6. Furthermore, to see the size of the magnetoresistance (MR) Figure 6.1b displays MR as a function of the magnetic field (over the resistivity). This figure shows clearly that below 20 K Ta_2PdSe_6 starts showing magnetoresistance that can go up to 26. More interestingly, it also shows that MR is roughly proportional to $H^{1.6}$.

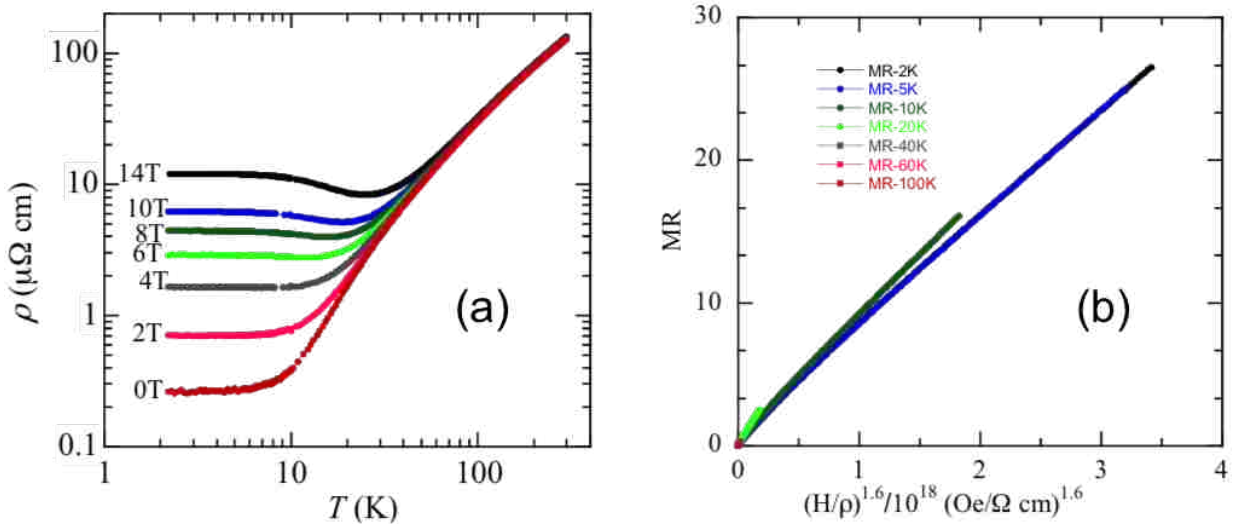

Figure 6.1: Experimental results of Ta_2PdSe_6 by Liu and Mao [61]. (a) Resistivity (ρ) Vs. temperature (T) for different external magnetic fields. (b) Magnetoresistance (MR) Vs. external magnetic (H) field for different sample temperatures. Note that the dots on the left corner describe data for 40 K, 60 K and 100 K that show no magnetoresistance.

In this Chapter, we are going to discuss the electronic structure of Ta_2PdSe_6 based on first-principles calculations and also describe what may be the mechanism behind the magnetoresistance of Ta_2PdSe_6. In order to do that we need the lattice parameters of Ta_2PdSe_6 as inputs to the density functional theory (DFT) calculations. However, there are not many experiments on Ta_2PdSe_6. Perhaps the earliest study on Ta_2PdSe_6 was conducted by Keszler et al. [130]. According to their report Ta_2PdSe_6 has a monoclinic structure (see Figure 6.2a) with $\alpha = \beta = 90^\circ$ and $\gamma = 130^\circ$ in the C2/m space group. The corresponding first Brillouin zone (BZ) is visualized in Figure 6.2b where a, Γ, c, and d are some of its high-symmetry points. The lattice constants p, q, r, respectively are 23.55, 23.05, and 6.38 in Bohrs. These parameters are the ones we used as inputs for our DFT calculations.

6.2 Methods

We used the DFT method to study the electronic structure of Ta_2PdSe_6 as implemented in WIEN2K [76] with a basis set of LAPW (see Section 2.1.4 for details.) We first applied

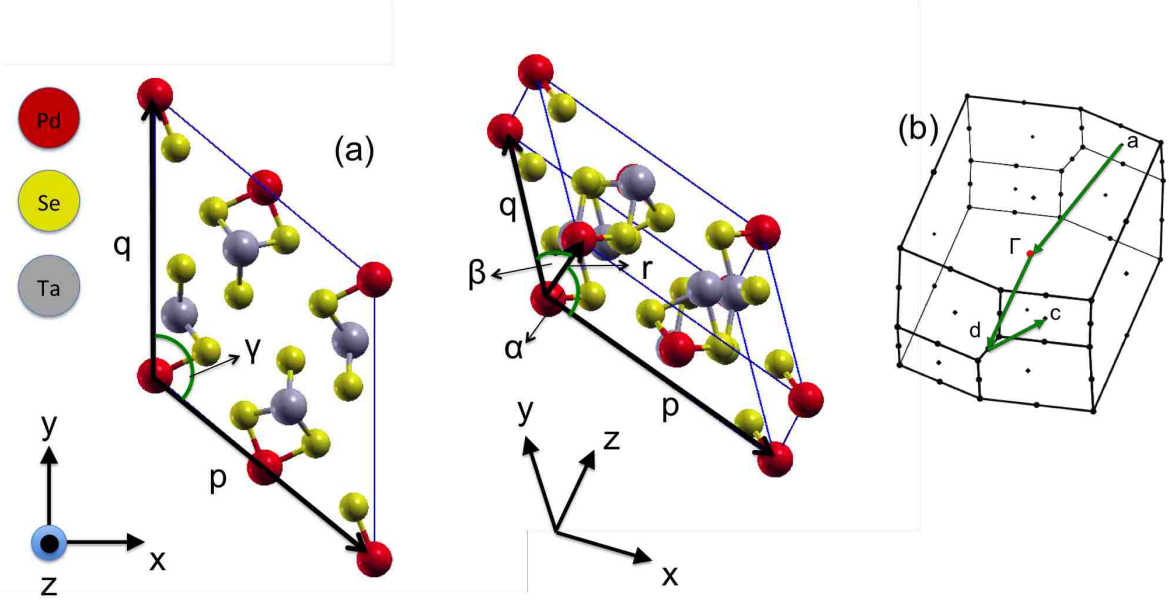

Figure 6.2: (a) Crystal structure of Ta_2PdSe_6 from two different perspectives. Red, yellow, and grey balls respectively represent palladium, selenium, and Tantalum. The lattice parameters p, q, r, respectively, are 23.55, 23.05, and 6.38 in Bohr with $\alpha = \beta = 90^\circ$ and $\gamma = 130^\circ$. (b) The first Brillouin zone of Ta_2PdSe_6 where dots represent all the high-symmetry points. Four high-symmetry points a, Γ, d, and c are chosen for plotting bandstructure.

the local-density approximation (LDA) potential into the calculation. Later on, to check the robustness of the result we used the generalized gradient approximation of Perdew-Burke-Ernzerhof for solids (PBESOL) [68], and modified Becke-Johnson potential (mBJ) [69]. The last one was used to see if the nature of the band gap changed. As we know LDA always underestimates the band gap in semiconductors, and thus it may happen that the nature of a system is mistakenly identified with LDA. If Ta_2PdSe_6 is a semiconductor, the use of mBJ will increase the band gap and thus help us reveal the true nature of Ta_2PdSe_6. Hence, the result from the mBJ calculation would add more confidence in the results. The self-consistent calculations were performed with a $14 \times 14 \times 4$ k-mesh in the first BZ.

Furthermore, due to limited time we did not relax the system to get optimized structure of the system and did not investigate the low-energy states around the Fermi level with the downfolding method [82]. These aspects might be used as motivations for future studies to give a more comprehensive picture of Ta_2PdSe_6, especially its magnetoresistance

mechanisms. As will be explained below, charge compensation is not enough to explain experimental data and thus there might be more than one mechanisms behind Ta_2PdSe_6 magnetoresistance.

6.3 Results and Discussion

Figure 6.3a shows Ta_2PdSe_6 bandstructure from the LDA calculation. As can be seen along the momentum (k)-path there exist two carrier pockets, hole and electron pockets. This is an indication that Ta_2PdSe_6 is semimetallic. Furthermore, the semimetallic character of Ta_2PdSe_6 can be verified more clearly by its density of states (DOS) which is plotted in Figure 6.3b. At the Fermi energy ($E_F = 0$ eV), the DOS is very small yet still finite; a sign of the existence of carrier pockets. The partial DOS of Ta in the inset of Figure 6.3b shows further that the states at the E_F are dominated by Ta-d character.

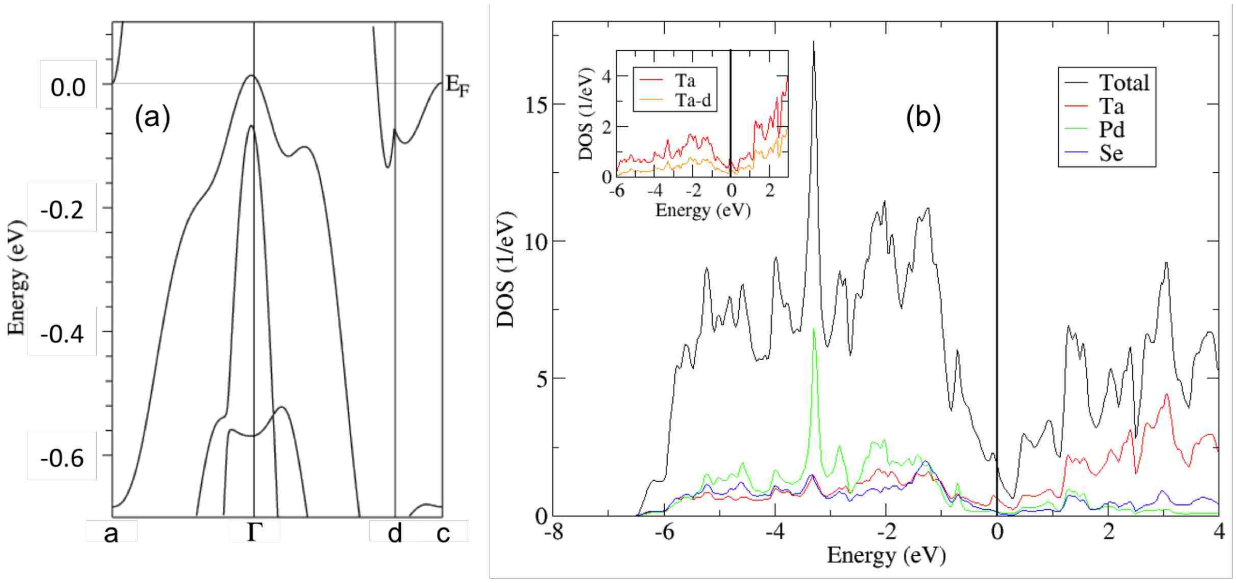

Figure 6.3: Ta_2PdSe_6 electronic structure. (a) Bandstructure. A hole pocket can be seen clearly around Γ and an electron pocket around d. (b) The total and partial density of states (DOS). The inset shows the partial DOS of Ta and Ta-d around the Fermi energy ($E_F = 0$).

To get a picture of the pockets in the three-dimensional momentum-space, we plot the Fermi surface (FS) in the first BZ (Figure 6.4a). As can be seen, two pockets are distant

in the the space and never cross each other. Moreover, if we extend the plot beyond the first BZ we can see that Ta_2PdSe_6 Fermi surface is essentially two-dimensional (2D), and thus anisotropic. The size of the Fermi surface is also quite sizable which could mean a semimetallic character against exchange-correlation potentials. We tested the robustness of the semimetallic character of Ta_2PdSe_6 by changing the exchange-correlation potentials to PBESOL and mBJ. The Fermi surface results of those two calculations are shown in Figure 6.4b and Figure 6.4c, respectively. As we can see the two carrier pockets persist. The Fermi surface obtained from PBESOL is essentially the same as the one from LDA. What is different is the size of the small hole pocket around the Γ point which is smaller in the PBESOL case. However, since its size is much smaller compared to the size of the entire hole pocket, the difference will not qualitatively change the nature of the system. Next, we compare the Fermi surface of mBJ and of LDA. We see that although the Fermi surface shape changes significantly the two pockets persist in the mBJ calculation, and thus it confirms the robustness of the semimetallic nature of Ta_2PdSe_6. Furthermore, since our system is essentially semimetallic, we will henceforth only consider the LDA result for further analysis.

As implied by the number of pockets in its electronic structures, Ta_2PdSe_6 has two types of charge carrier, namely n and p-types (electrons and holes, respectively). To determine the density of the electrons(holes) we integrate the band-decomposed DOS of the electron(hole)

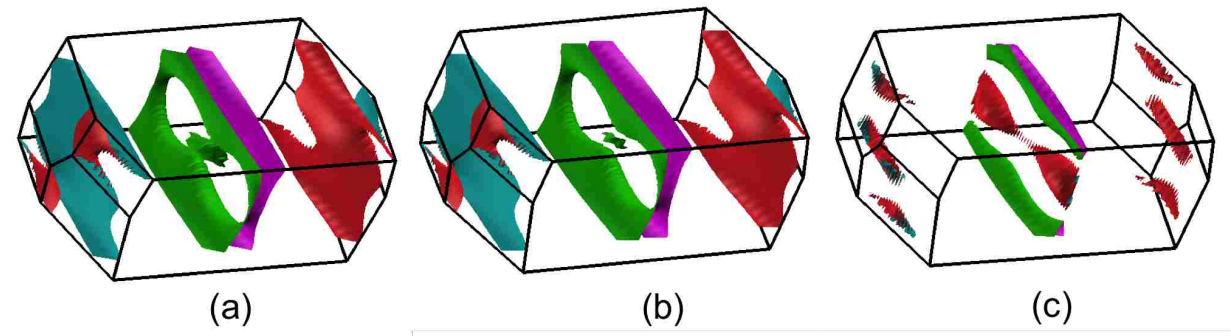

Figure 6.4: Ta_2PdSe_6 Fermi surface of (a) LDA, (b) PBESOL, and (c) mBJ calculations.

pocket from E_F to the conduction(valence) band minimum(maximum). From the LDA calculation, we got exactly the same electron and hole concentrations, $n = p = 3.5 \times 10^{20}$ cm^{-3}.

Having determined the nature of Ta_2PdSe_6 and its carrier densities, we now have a very clear hint of what may become the mechanism behind the magnetoresistance of Ta_2PdSe_6. In a two-band model the magnetoresistance (MR) is given by [132]

$$MR = \frac{\sigma\sigma' \left(\frac{\sigma}{n} + \frac{\sigma'}{p}\right)^2 \left(\frac{H}{e}\right)^2}{(\sigma + \sigma')^2 + \sigma^2\sigma'^2 \left(\frac{1}{n} - \frac{1}{p}\right)^2 \left(\frac{H}{e}\right)^2} , \tag{6.1}$$

where σ and σ', respectively, are the conductivity of electrons and holes. Equation (6.1) further says that when $n = p$, MR will be exactly linearly proportional to H^2. This result is pretty close to the experimental data (Figure 6.1b) although it is not really accurate. Based on this result, we, therefore, propose that the charge compensation is the mechanism responsible for the Ta_2PdSe_6 magnetoresistance. However, since this mechanism based on two-band model is not so accurate to the experimental data, we believe there might be some other mechanisms that drive Ta_2PdSe_6 magnetoresistance.

6.4 Conclusion

We have calculated the electronic structure of Ta_2PdSe_6 with the DFT method. According to our DFT calculations Ta_2PdSe_6 is a semimetal and its semimetallic nature is robust against several DFT exchange-correlation potentials. Furthermore, we also found that the electron and hole densities are equal. This result implies that, following the two-band model for magnetoresistance, the mechanism to explain the Ta_2PdSe_6 magnetoresistance is the charge compensation. However, due to the magnetoresistance dependence on the magnetic field obtained from the two-band model that is not exactly commensurate to its experimental counterpart, we suggest that there might be some other mechanisms involved behind Ta_2PdSe_6 magnetoresistance.

Chapter 7
Summary and Outlook

We have investigated several issues on diluted magnetic semiconductors (DMS) and the magnetoresistive material Ta_2PdSe_6 by means of first-principles and model Hamiltonian methods. The first-principles method used in this work is the density-functional theory with the LAPW basis set as implemented in the WIEN2K package [76], whereas the model Hamiltonian implemented is a spin-fermion model which is solved within the dynamical mean-field theory (DMFT) and the typical medium theory (TMT). The investigation is very critical for further studies in spintronic materials.

In Chapter 4, we have resolved the Mn valence in (Ga,Mn)N. We found the Mn valence is 2+ but with a non-atomic spin of $4\mu_B$, illustrating the inadequacy of ionic valence in an atomic picture. We then demonstrated the feasibility of multiple pictures to describe the low-energy physics of (Ga,Mn)N, namely the effective d^4 and d^5 pictures. The effective d^4 picture (naturally with $S = 4$) is suitable for studying local instabilities and excitations, whereas the effective d^5 picture can be used for future studies of long-range magnetic order, non-local magnetic correlation, and other transport properties. Our study not only resolves one of the outstanding key puzzles in the field, but also emphasizes the general need for multiple effective pictures to describe the rich low-energy physics in many-body systems in general.

Furthermore, we expect that our d^5 model will resolve important issues in (Ga,Mn)N such as the magnetic ordering and the Anderson localization. We particularly show a few novel physical effects beyond previous considerations in the field, such as a very huge local potential that drives Anderson localization in DMS and spin-dependent hopping terms that determine magnetic exchange and magnetic order in DMS. Moreover, our d^5 model can also be easily implemented for other III-V DMS with different dopants; i.e. for any III-V DMS

we can derive a similar d^5 Hamiltonian with the same first-principles procedures. With these d^5 Hamiltonians we can do a few things to deepen our understanding about III-V DMS, for instance we can analyze how parameters of the d^5 Hamiltonian change as the host crystal and the dopant change. By doing that we can see which configuration of III-V semiconductor and dopant provides the best environment for ferromagnetic order. Once we have determined the Hamiltonian we can step further to solve the Hamiltonian with man-body techniques. The solution will provide insights into ferromagnetism in III-V DMS and thus a more general picture of III-V DMS.

As the first step to understanding Anderson localization in DMS, we discuss in Chapter 5 our investigation of this issue using a simple spin-fermion model which was then solved using TMT. We observed the impurity band-valence band crossover in DMS as found in previous studies [125, 126]. By looking at the evolution of the hybridization, we also observed the metal-insulator Anderson localization transition which has never previously been shown in any theoretical DMS studies. Furthermore, the existence of Anderson localization has suppressed the ferromagnetic order in DMS. Our result agrees with previous studies [58] that to escape the localization a DMS system should be doped at concentration greater than a critical value. This demonstrates the power of TMT to reveal Anderson localization in DMS even with only a simple model.

In the future, the study of Anderson localization in DMS can be much improved using more sophisticated many-body methods like typical-medium dynamical cluster approximation (TMDCA) [133]. By using cluster approximations we hope to capture non-local effects that may contribute to the localization. In addition to the use of more advanced many-body methods, we can also use more realistic Hamiltonians like our d^5 Hamiltonian to study Anderson localization. However, as most computational codes of many-body methods are still incapable of handling multiorbital Hamiltonians, we have to first develop these computational codes capable of processing multiorbital Hamiltonians. By using more realistic Hamiltonians we expect that future theoretical studies can explain experimental

results not only qualitatively but also quantitatively.

Finally, we also reported our study of Ta_2PdSe_6. This material has been shown experimentally to have a quite large magnetoresistance [61]. By means of the DFT method, we showed that Ta_2PdSe_6 is semimetallic with two kinds of carriers with the same density. By connecting our finding to the two-band model of the magnetoresistance we propose that the mechanism behind Ta_2PdSe_6 magnetoresistance is charge compensation. However, since the result of the Ta_2PdSe_6 magnetoresistance dependence on magnetic field does not quite agree with our result, there might be some other mechanisms besides charge compensation that cannot be captured by present DFT calculations.

Nevertheless, we hope that our study can stimulate more theoretical and experimental studies of Ta_2PdSe_6 to better understand its magnetoresistance and mechanisms behind it and also perhaps to discover its potential applications for spintronics. Particularly, it would be interesting to include some factors such as geometry optimization and spin-orbit coupling in DFT calculations of Ta_2PdSe_6 and to see how these factors modify the present result. Furthermore, to investigate some other mechanism involved in Ta_2PdSe_6 magnetoresistance one may need to consider the downfolding method [81, 82] to get an effective Hamiltonian that can be used to calculate the carrier densities and magnetoresistance more accurately.

References

[1] M. N. Baibich, J. M. Broto, A. Fert, F. Nguyen Van Dau, and F. Petroff, Phys. Rev. Lett. **61**, 2472 (1988).

[2] S. A. Solin, Scientific American, July, 71 (2004).

[3] J. Daughton, J. Brown, E. Chen, R. Beech, A. Pohm, and W. Kude, IEEE Trans. Magn. **30**, 4608 (1994).

[4] M. Tondra, J. M. Daughton, D. Wang, R. S. Beech, A. Fink, and J. A. Taylor, J. Appl. Phys. **83**, 6698 (1998).

[5] G. A. Prinz, Science **282**, 1660 (1998).

[6] S. Das Sarma, Am. Scientist **89**, 516-523 (2001).

[7] I. Žutić, J. Fabian, and S. Das Sarma, Appl. Phys. Lett. **79**, 1558-1560 (2001).

[8] B. Endres, M. Ciorga, M. Schmid, M. Utz, D. Bougeard, D. Weiss, G. Bayreuther, and C. H. Back, Nature Commun. **4**, 2068 (2013).

[9] Y. Ohno, D. K. Young, B. Beschoten, F. Matsukura, H. Ohno, and D. D. Awschalom, Nature **402**, 790-792 (1999).

[10] S. A. Wolf, D. D. Awschalom, R. A. Buhrman, J. M. Daughton, S. von Molnár, M. L. Roukes, A. Y. Chtchelkanova, and D. M. Treger, Science **294**, 1488 (2001).

[11] S. J. Pearton, C. R. Abernathy, G. T. Thaler, R. M. Frazier, D. P. Norton, F. Ren, Y. D Park, J. M. Zavada, I. A. Buyanova, W. M. Chen, and A. F. Hebard, J. Phys.: Condens. Matter **16**, R209–R245 (2004).

[12] J. W. Dong, L. C. Chen, C. J. PalmstrØm, R. D. James, and S. McKernan, Appl. Phys. Lett. **75**, 1443 (1999).

[13] S. M. Watts, S. Wirth, S. von Molnár, A. Barry and J. M. D. Coey, Phys. Rev. B **61**, 9621 (1999).

[14] J. M. D. Coey , M. Viret, and S. von Molnár, Adv. Phys. **48**, 169 (1999).

[15] S. Methfessel and D. C. Mattis, Handb. Phys. **18**, 389 (1968).

[16] A. Mauger and C. Godart, Phys. Rep. **141**, 51 (1986).

[17] P. K. Baltzer, P. J. Wojtowicz, M. Robbins, Phys. Rev. **151**, 367 (1966).

[18] P. G. Steeneken et al., Phys. Rev. Lett. **88**, 047201 (2002).

[19] J. Lettieri et al., App. Phys. Lett. **83**, 975 (2003).

[20] V. A. Ivanov, T. G. Aminov, V. M. Novotortsev, and V. T. Kalinnikov, Russian Chemical Bulletin **53**, 2357 (2004).

[21] J. K. Furdyna and J. Kossut (Eds.), Semiconductors and semimetals, Volume **25**, Academic Press, San Diego (1988).

[22] T. Story, R. R. Galazka, R. B. Frankel and P. A. Wolff, Phys. Rev. Lett. **56**, 777 (1986).

[23] D. Ferrand, J. Cibert, A. Wasiela, C. Bourgognon, S. Tatarenko, G. Fishman, T. Andrearczyk, J. Jaroszynski, S. Kolesnik, T. Dietl, B. Barbara, D. Dufeu, Physical Review B **63**, 085201 (2001).

[24] S. Koshihara, A. Oiwa, M. Hirasawa, S. Katsumoto, Y. Iye, C. Urano, H. Takagi, and H. Munekata, Phys. Rev. Lett. **78**, 4617 (1997).

[25] F. Matsukura, H. Ohno, and T. Dietl, *in Handbook of Magnetic Materials*, edited by K. H. J. Buschow (ElsevierAmsterdam), Vol. **14**, p. 1 (2002).

[26] H. Ohno, A. Shen, F. Matsukura, A. Oiwa, A. Endo, S. Katsumoto, and Y. Iye, Appl. Phys. Lett. **69**, 363 (1996).

[27] MacDonald, A. H., P. Schiffer, and N. Samarth, Nat. Mater. **4**, 195 (2005).

[28] T. Dietl, H. Ohno, and F. Matsukura, Phys. Rev. B **63**, 195205 (2001).

[29] T. Dietl, Semicond. Sci. Technol. **17**, 377 (2002).

[30] B. Lee, T. Jungwirth, and A. H. MacDonald, Semicond. Sci. Technol. **17**, 393 (2002).

[31] S. Sanvito, G. Theurich, and N. A. Hill, J. Supercond. **15**, 85 (2002).

[32] K. Sato, and H. Katayama-Yoshida, Semicond. Sci. Technol. **17**, 367 (2002).

[33] T. Jungwirth, J. Sinova, J. Mašek, J. Kučera, A. H. MacDonald, Rev. Mod. Phys. **78**, 809-864 (2006).

[34] T. Jungwirth, J. Wunderlich, V. Novák and K. Olejník, B. L. Gallagher, R. P. Campion, K. W. Edmonds, A. W. Rushforth, A. J. Ferguson, P. Němec, Rev. Mod. Phys. **86**, 855 (2014).

[35] H. Amano, N. Sawaki, I. Akasaki, and Y. Toyoda, Appl. Phys. Lett., **48**, 353-355 (1986).

[36] I. Akasaki, H. Amano, H. Murakami, M. Sassa, H. Kato, and K. Manabe, Journal of Crystal Growth **128**, 379-383 (1993).

[37] S. Nakamura, T. Mukai, and M. Senoh, Appl. Phys. Lett. **64**, 1687 (1994).

[38] D. Chen, Z. Ding, S. Yao, W. Hua, K. Wang, T. Chen, Nucl. Instr. and Meth. in Phys. Res. B, **266**, 2797-2800 (2008).

[39] M. Zając, J. Gosk, M. Kamińska, A. Twardowski, T. Szyszko, and S. Podsiadło, Appl. Phys. Lett. **79**, 2432 (2001).

[40] S. Granville, B. J. Ruck, F. Budde, H. J. Trodahl, and G. V. M. Williams, Phys. Rev. B **81**, 184425 (2010).

[41] S. Dhar, O. Brandt, A. Trampert, K. J. Friedland, Y. J. Sun ,and K. H. Ploog, Phys. Rev. B **67**, 165205 (2003).

[42] M. E. Overberg, C. R. Abernathy, S. J. Pearton, N. A. Theodoropoulou, K. T. McCarthy, and A. F. Hebard, Appl. Phys. Lett. **79**, 1312 (2001).

[43] S. Stefanowicz, G. Kunert, C. Simserides, J. A. Majewski, W. Stefanowicz, C. Kruse, S. Figge, Tian Li, R. Jakieła, K. N. Trohidou, A. Bonanni, D. Hommel, M. Sawicki, and T. Dietl1, Phys. Rev. B **88**, 081201(R) (2013).

[44] G. T. Thaler, M. E. Overberg, B. Gila, R. Frazier, C. R. Abernathy, S. J. Pearton, J. S. Lee, S. Y. Lee, Y. D. Park, Z. G. Khim, J. Kim, and F. Ren, Appl. Phys. Lett. **80**, 3964 (2002).

[45] M. L. Reed, N. A. El-Masry, H. H. Stadelmaier, M. K. Ritums, M. J. Reed, C. A. Parker, J. C. Roberts, and S. M. Bedair, Appl. Phys. Lett. **79**, 3473 (2001).

[46] T. Sasaki, S. Sonoda, Y. Yamamoto, K.-I. Suga, S. Shimizu, K. Kindo, and H. Hori, J. Appl. Phys. **91**, 7911 (2002).

[47] C. Liu, F. Yun and H. Morkoç, J. Mater. Sci. Mater. Electron. **16**, 555 (2005).

[48] K. Sato, L. Bergqvist, J. Kudrnovský, P. H. Dederichs, O. Eriksson, I. Turek, B. Sanyal, G. Bouzerar, H. Katayama-Yoshida, V. A. Dinh, T. Fukushima, H. Kizaki, R. Zeller, Rev. Mod. Phys. **82**, 1633–1690 (2010).

[49] M. Abolfath, T. Jungwirth, J. Brum and A. H. MacDonald, Phys. Rev. B **63**, 054418 (2010).

[50] C. Zener, Phys. Rev. **81**, 440, (1951).

[51] T. Hayashi, Y. Hashimoto, S. Katsumoto, and Y. Iye, Appl. Phys. Lett. **78**, 1691 (2001).

[52] K. W. Edmonds, K. Y. Wang, R. P. Campion, A. C. Neumann, N. R. S. Farley, B. L. Gallagher, and C. T. Foxon, Appl. Phys. Lett. **81** 4991 (2002).

[53] K. M. Yu, W. Walukiewicz, T. Wojtowicz, I. Kuryliszyn, X. Liu, Y. Sasaki, and J. K. Furdyna, Phys. Rev. B **65**, 201303(R) (2002).

[54] L. P. Rokhinson, Y. Lyanda-Geller, Z. Ge, S. Shen, X. Liu, M. Dobrowolska, J. K. Furdyna, Phys. Rev. B **76**, 161201(R), (2007).

[55] C. Zener, Phys. Rev. **82**, 403-405, (1951).

[56] N. Furukawa, arXiv:cond-mat/9812066 (1998).

[57] K. Sato, P. H. Dederichs, H. Katayama-Yoshida, and J. Kudrnovský, J. Phys.: Condens. Matter **16**, S5491 (2004).

[58] A. Richardella, P. Roushan, S. Mack, B. Zhou, D. A. Huse, D. D. Awschalom, and A. Yazdani, Science **327**, 665 (2010).

[59] W. Thomson, Proc. Royal Soc. London **8**, 546–550 (1856).

[60] G. H. Jonker and J. H. Van Santen, Physica **16**, 337-349 (1950).

[61] J. Liu, R. Nelson, et al., Tulane University, Louisiana State University, and Brookhaven National Laboratory (in preparation.)

[62] J. P. Perdew and A. Zunger Phys. Rev. B **23** 5048 (1981).

[63] S. H. Vosko, L. Wilk, and M. Nusair, Can. J. Phys. **58**, 1200 (1980).

[64] D. M. Ceperley and B. J. Alder Phys. Rev. Lett. **45**, 566 (1980).

[65] D. C. Langreth and M. J. Mehl Phys. Rev. B **28**, 1809 (1983).

[66] A. D. Becke, Phys. Rev. A **38**, 3098 (1988).

[67] J. P. Perdew, J. A. Chevary, S. H. Vosko, Koblar A. Jackson, Mark R. Pederson, D. J. Singh, and C. Fiolhais, Phys. Rev. B **46**, 6671 (1992).

[68] J.P. Perdew et al., Phys. Rev. Let. **100**, 136406 (2008).

[69] F. Tran and P. Blaha, Phys. Rev. Lett. **102**, 226401 (2009).

[70] A. D. Becke and E. R. Johnson, The Journal of Chemical Physics **124**, 221101 (2006)

[71] V.I. Anisimov, J. Zaanen, and O.K. Andersen, Phys. Rev. B **44**, 943 (1991).

[72] V.I. Anisimov, I.V. Solovyev, M.A. Korotin, M.T. Czyżyk, and G.A. Sawatzky, Phys. Rev. B **48**, 16929 (1993).

[73] M. T. Czyżyk and G. A. Sawatzky, Phys. Rev. B **49**, 14211 (1994)

[74] J. C. Slater Phys. Rev. **51**, 846 (1937).

[75] O. K. Andersen Phys. Rev. B **12**, 3060 (1975).

[76] P. Blaha *et al.*, Comput Phys. Commun. **147**, 71 (2002).

[77] Tom Berlijn, Dmitri Volja, and Wei Ku, Phys. Rev. Lett. **106**, 077005 (2011).

[78] Tom Berlijn, Chia-Hui Lin, William Garber, and Wei Ku **108**, 207003 (2012).

[79] V. I. Anisimov et al. Phys. Rev. B **71**, 125119 (2005).

[80] C. Weber, K. Haule, and G. Kotliar Phys. Rev. B **78** 134519 (2008).

[81] N. Marzari and D. Vanderbilt Phys. Rev. B **56**, 12847 (1997).

[82] W. Ku et al. Phys. Rev. Lett. **89**, 167204 (2002).

[83] W.-G. Yin, D. Volja, and W. Ku Phys. Rev. Lett. **96**, 116405 (2006).

[84] R. L. Barnett, A. Polkovnikov, E. Demler, W.-G. Yin, and W. Ku, Phys. Rev. Lett. **96**, 026406 (2006).

[85] C.-C. Lee, W.-G. Yin, and W. Ku Phys. Rev. Lett. **103** 267001 (2009).

[86] A. C. Walters, T. G. Perring, J. S. Caux, A. Savici, G. D. Gu, C. C. Lee, W. Ku, and I. Zaliznyak Nat. Phys. **5**, 867 (2009).

[87] I. Mayer International Journal of Quantum Chemistry **90**, 63 (2002).

[88] P. W. Anderson, Phys. Rev. **124**, 41 (1961).

[89] A. Georges, arXiv:cond-mat/0403123 (2004).

[90] D. Vollhardt, arXiv:1004.5069 (2010).

[91] P. W. Anderson, Phys. Rev. **109**, 1492 (1958).

[92] V. Dobrosavljević, arXiv:cond-mat/0106282v2 (2003).

[93] R. Y. Korotkov, J. M. Gregie, B. W. Wessels, Physica B **308**, 30 (2001).

[94] R. Y. Korotkov, J. M. Gregie, B. W. Wessels ,Appl. Phys. Lett. **80**, 1731 (2002).

[95] K. S. Burch, D. D. Awschalomb, and D. N. Basov, J. Magn. Magn. Mater. **320**, 3207-3228 (2008).

[96] E. Kulatov, H. Nakayama, H. Mariette, H. Ohta, and Y. A. Uspenskii, Phys. Rev. B **66**, 045203 (2002).

[97] B. Sanyal, O. Bengone, and S. Mirbt, Phys. Rev. B **68**, 205210 (2003).

[98] L. M. Sandratskii, P. Bruno, and J. Kudrnovský, Phys. Rev. B **69**, 195203 (2004).

[99] M. Wierzbowska, D. Sanchez-Portal, and S. Sanvit, Phys. Rev. B **70**, 235209 (2004).

[100] J. Kang, K. J. Chang, and H. Katayama-Yoshida, J. Superconductivity: Incorporating Novel Magnetism **18**, 55 (2005).

[101] Priya Mahadevan and Alex Zunger, Phys. Rev. B **69**, 115211, (2004).

[102] J. Schneider, U. Kaufmann, W. Wilkening, and M. Baeumler, and F. Kohl, Phys. Rev. Lett. **59**, 240 (1987).

[103] X. Biquard, O. Proux, J. Cibert, D. Ferrand, H. Mariette, R. Giraud, and B. Barbara, Journal of Superconductivity: Incorporating Novel Magnetism, **16**, 127 (2003).

[104] A. Titov et al., Phys. Rev. B **72**, 115209 (2005).

[105] W. Stefanowicz et al., Phys. Rev. B **81**, 235210 (2010).

[106] T. Graf, M. Gjukic, M. S. Brandt, M. Stutzmann, and O. Ambacher, Appl. Phys. Lett. **81**, 5159 (2002).

[107] T. Graf, M. Gjukic, M. Hermann, M. S. Brandt, M. Stutzmann, L. Görgens, J. B. Philipp, and O. Ambacher, Journal of Applied Physics **93**, 9697 (2003).

[108] Y. L. Soo et al., Appl. Phys. Lett. **79**, 3926 (2001).

[109] K. W. Edmonds et al., Journal of Applied Physics **95**, 7166 (2004).

[110] J. I. Hwang et al., Phys. Rev. B **72**, 085216 (2005).

[111] Xuan Luo and Richard M. Martin, Phys. Rev. B **72**, 035212 (2005).

[112] A. Boukortt and R. Hayn and F. Virot, Phys. Rev. B **85**, 033302 (2012).

[113] B. C. Larson et al., Phys. Rev. Lett. **99**, 026401 (2007).

[114] F. C. Zhang and T. M. Rice, Phys. Rev. B **37**, 3759 (1988).

[115] W.-G. Yin and W. Ku, Phys. Rev. B **79**, 214512(R) (2009).

[116] C.-C. Lee et al., Phys. Rev. B **82**, 081106(R) (2010).

[117] C.-C. Lee et al., Phys. Rev. Lett. **111**, 157401 (2013).

[118] P. Abbamonte et al., PNAS **105**, 12159 (2008).

[119] X. Y. Cui, B. Delley, J. Freeman, and C. Stampfl, Phys. Rev. B **76**, 045201 (2007).

[120] V. J. Emery and G. Reiter, Phys. Rev. B **38**, 4547 (1988).

[121] S. Ohya, K. Takata, and M. Tanaka, Nature Physics **7**, 342 (2011).

[122] M. Dobrowolska et al., Nature Materials **11**, 444 (2012).

[123] M. E. Flatte, Nat. Phys. **7**, 285 (2011).

[124] N. Samarth, Nature Materials **11**, 360 (2012).

[125] F. Popescu, C. Sen, E. Dagotto, and A. Moreo, Phys. Rev. B **76**, 85206, (2007).

[126] M. Takahashi and K. Kubo, J. Phys. Soc. Jpn **72**, 2866 (2003).

[127] P. Soven, Phys. Rev., **156**, 809 (1967).

[128] M. Janssen, Int. J. Mod. Phys. B **8**, 943, (1994).

[129] E. Crow and K. Shimizu, Log-Normal Distribution–Theory and Applications.: Marcel Dekker, NY, (1988).

[130] D. A. Keszler et al.; Inorg. Chem. **24**, 3063-3067 (1985).

[131] J. P. Perdew, S. Burke, and M. Ernzerhof, Phys. Rev. Let. **77**, 3865 (1996).

[132] F. Duan and J. Guojun, *Introduction to Condensed Matter Physics*, World Scientific Publishing Co. Pte. Ltd, Vol. 1, p. 215 (2005).

[133] C. E. Ekuma, et al., Phys. Rev. B **89**, 081107(R) (2014).

Appendix A
The Derivation of The Effective d^5 Hamiltonian of (Ga,Mn)N

The following derivation is to illustrate how "high-energy" degrees of freedom in (Ga,Mn)N are integrated out while the "low-energy" ones are retained to form the effective low-energy potentials, i.e. the spin-independent and -dependent potentials. To this end we perform 2^{nd} order perturbation theory on a simple model Hamiltonian consisting of 5 Mn-d orbitals and 4 N-sp^3 orbitals pointing towards the Mn. The resulting coupling constants of this calculation should, of course, not be taken too literally. Instead, they serve the purpose of providing the most relevant terms in the low-energy effective Hamiltonian, whose coefficients are to be determined from first-principles analysis, as shown in the manuscript.

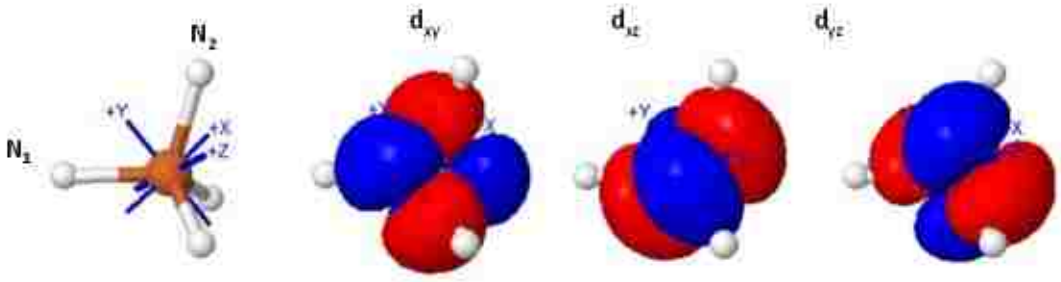

Figure S1: Model of Mn-t_{2g} orbitals in tetrahedral crystal field of surrounding N atoms obtained from `http://wwwchem.uwimona.edu.jm:1104/courses/CFT_Orbs.html`.

The Hamiltonian is given by:

$$
\begin{aligned}
H_{\text{bare}} = & \sum_{mm'\sigma} \left(t^{mm'} c^{\dagger}_{m\sigma} c_{m'\sigma} + h.c. \right) + \sum_{l\sigma} \varepsilon_l n^d_{l\sigma} \\
& + U \sum_{l} n^d_{l\uparrow} n^d_{l\downarrow} + U' \sum_{l<l'\sigma\sigma'} n^d_{l\sigma} n^d_{l'\sigma'} - J \sum_{l<l'\sigma\sigma'} d^{\dagger}_{l\sigma} d^{\dagger}_{l'\sigma'} d_{l'\sigma} d_{l\sigma'} \\
& + \sum_{\langle m,l\rangle\sigma} \left(V_{\langle m,l\rangle} c^{\dagger}_{m\sigma} d_{l\sigma} + h.c. \right)
\end{aligned} \tag{A.1}
$$

where,

m, m' : indices of N-sp^3 orbitals pointing toward Mn,

l, l' : indices of Mn-d orbitals,

σ, σ' : spin indices,

$t^{mm'}$: ($\equiv t$) N-sp^3 to N-sp^3 hopping parameter for $m \neq m'$,

$t^{mm'}$: ($\equiv \varepsilon_m$) on-site energy of N-sp^3 orbitals for $m = m'$,

ε_l : on-site energy of Mn-d orbitals,

U : intra-orbital Coulomb interaction of the Mn-d orbitals,

U' : inter-orbital Coulomb interaction of the Mn-d orbitals,

J : Hund's coupling of Mn-d orbitals,

$V_{\langle m,l\rangle}$: hybridization parameter,

$c^{\dagger}, c$: creation and annihilation operators of N-sp^3 electrons,

$d^{\dagger}, d$: creation and annihilation operators of Mn electrons,

n : $c^{\dagger}c$,

n^d : $d^{\dagger}d$.

Moreover, due to the size of the Hund's coupling J we assume that the spin of the e_g electrons is always aligned with one of the t_{2g} electrons. Finally, we specifically deal with

a system with only one doped hole.

Now consider the Hamiltonian (A.1) when the hybridization is turned off ($V_{\langle m,t_{2g}\rangle} = 0$). In this particular situation we can group all states into two disconnected Hilbert spaces: low- and high-energy subspaces. The low-energy Hilbert space contains a hole in the N-sp^3 orbitals while the Mn-t_{2g} and e_g orbitals are half-filled and in the high-spin configuration ($S = \frac{5}{2}$) with energy $E_{d^5} = 3\varepsilon_m + 5\varepsilon_l + \dfrac{5!}{2!3!}(U' - J)$, where factor 3 comes from the number of occupied N orbitals around Mn, the factor 5 counts the number of occupied Mn-d orbitals, and the factor of $10 = 5!/(2!\,3!)$ is the number of Mn-d orbitals pairs. Meanwhile, the rest of the states are part of the high-energy Hilbert space; in particular the atomic d^4 states with a hole localized on the Mn site and energy $E_{d^4} = 4\varepsilon_m + 4\varepsilon_l + 6\,(U' - J)$, where the factor of $6 = 4!/(2!\,2!)$ is the number of Mn-d pairs, belongs to the high-energy sector. The energy difference between the high- (d^4) and low-energy (d^5) Hilbert spaces becomes $\Delta_E = E_{d^4} - E_{d^5} = \varepsilon_m - \varepsilon_l - 4\,(U' - J)$. When the hybridization is turned on ($V_{\langle m,t_{2g}\rangle} \neq 0$) the low- and high-energy states are mixed. The task is then to extract the change in the low-energy Hilbert space due to the hybridization between d^4 & d^5 degrees of freedom.

The change in the energy of d^5 to 2$^{\text{nd}}$ order in perturbation theory is given by[1]

$$\langle\beta|\Delta|\alpha\rangle = \langle\beta|\hat{V}|\alpha\rangle - \sum_{\mu} \frac{\langle\beta|\hat{V}|\mu\rangle\langle\mu|\hat{V}|\alpha\rangle}{\Delta_E} \quad , \tag{A.2}$$

where

$$\begin{aligned}
&|\alpha\rangle, |\beta\rangle : \text{states in the low-energy } d^5 \text{ Hilbert space,}\\
&|\mu\rangle : \text{states in the high-energy } d^4 \text{ Hilbert space,}\\
&\hat{V} : \text{the hybridization operator} = \sum_{ml\sigma} \left(V_{\langle m,t_{2g}\rangle} c^{\dagger}_{m\sigma} d_{l\sigma} + h.c.\right),\\
&\Delta_E : \text{energy difference between the high- } (d^4) \text{ and low-energy } (d^5) \text{ Hilbert space.}
\end{aligned} \tag{A.3}$$

[1] K. Gottfried and T.-M. Yan, *Quantum Mechanics: Fundamentals, 2nd ed.*, 2003.

Furthermore, because the hybridization only connects the low-and high-energy terms the first term in Eq. (A.2) vanishes.

We particularly want to integrate out the atomic d^4 states ($|\mu\rangle$ states) and keep the effective d^5 states ($|\alpha\rangle$, $|\beta\rangle$). The d^4 states are formed when the hole hops to the Mn-t_{2g} orbitals whereas the hole is located effectively in the N-sp^3 orbitals for the d^5 states. If $|m\sigma, m_s\rangle$ denote $|\alpha\rangle$ and $|\beta\rangle$; i.e. representing orbital (m), and spin (σ) state of the hole and the projected spin state of Mn (m_s), we can group the different components of the second term of Eq. (A.2) into four contributions, all of them involving virtual hopping to Mn-t_{2g} orbitals (virtually forming a d^4 state):

(a) low-energy states in which the hole stays in the same N-sp^3 orbital without exchanging its spin with Mn; i.e. $\langle\beta|\Delta|\alpha\rangle = \sum_{\mu} \frac{\langle m\sigma, m_s|\hat{V}|\mu\rangle\langle\mu|\hat{V}|m\sigma, m_s\rangle}{\Delta_E}$,

(b) low-energy states in which the hole stays in the same N-sp^3 orbital but exchanges its spin with Mn; i.e. $\langle\beta|\Delta|\alpha\rangle = \sum_{\mu} \frac{\langle m\sigma', m'_s|\hat{V}|\mu\rangle\langle\mu|\hat{V}|m\sigma, m_s\rangle}{\Delta_E}$,

(c) low-energy states in which the hole hops from one N-sp^3 to another N-sp^3 without spin exchange; i.e.
$\langle\beta|\Delta|\alpha\rangle = \sum_{\mu} \frac{\langle m'\sigma, m_s|\hat{V}|\mu\rangle\langle\mu|\hat{V}|m\sigma, m_s\rangle}{\Delta_E}$,

(d) low-energy states in which the hole hops from one N-sp^3 to another N-sp^3 with spin exchange; i.e.
$\langle\beta|\Delta|\alpha\rangle = \sum_{\mu} \frac{\langle m'\sigma', m'_s|\hat{V}|\mu\rangle\langle\mu|\hat{V}|m\sigma, m_s\rangle}{\Delta_E}$.

Furthermore, we notice there are three possible Mn-t_{2g} orbitals where the hole can hop from an initial N-sp^3 orbital to form a virtual d^4 state ($|\mu\rangle$). For (a) and (b) these three possibilities give a factor of 3 to the calculation. However, they only give a factor of 1 for (c) and (d) due to the opposite sign that some of the hybridization factors have. For instance, Fig. SS1 shows that the hopping from N_1-sp^3 to N_2-sp^3 via d_{xz} will have an opposite sign of those via d_{xy} and d_{yz}, since the lobes pointing towards N_1 and N_2 are both positive for

d_{xz}, while they change sign for d_{xy} and d_{yz}.

$$\begin{aligned}\langle \mathrm{N}_1 sp_a^3\sigma', m_s'|\hat{V}|d_{xy}^4\rangle\langle d_{xy}^4|\hat{V}|\mathrm{N}_2 sp_b^3\sigma, m_s\rangle &= -\langle \mathrm{N}_1 sp_a^3\sigma', m_s'|\hat{V}|d_{xz}^4\rangle\langle d_{xz}^4|\hat{V}|\mathrm{N}_2 sp_b^3\sigma, m_s\rangle \\ &= \langle \mathrm{N}_1 sp_a^3\sigma', m_s'|\hat{V}|d_{yz}^4\rangle\langle d_{yz}^4|\hat{V}|\mathrm{N}_2 sp_b^3\sigma, m_s\rangle,\end{aligned} \tag{A.4}$$

where $|d_\nu^4\rangle$ denotes a particular t_{2g} orbital where the hole virtually hops into.

Next we show that by calculating some elements of

$$\Delta = -\sum_\mu \frac{\hat{V}|\mu\rangle\langle\mu|\hat{V}}{\Delta_E}, \tag{A.5}$$

we can compactly express Δ using the second-quantized form:

$$\Delta = \sum_{mm'\sigma} T^{mm'}\tilde{c}_{m\sigma}^\dagger\tilde{c}_{m'\sigma} + \sum_{\substack{mm'\\ \sigma\sigma'}} J^{mm'}\tilde{c}_{m\sigma}^\dagger\boldsymbol{\tau}_{\sigma\sigma'}\tilde{c}_{m'\sigma'}\cdot\boldsymbol{S} \;+\; h.c.\;, \tag{A.6}$$

Here $\boldsymbol{S}$, $\boldsymbol{\tau}_{\sigma\sigma'}$, and $\tilde{c}_{m\sigma}^\dagger$ ($\tilde{c}_{m\sigma}$) are, respectively, the quantum Mn spin-$\frac{5}{2}$ vector located at the origin, the Pauli matrices, and the creation (annihilation) operator of quasiparticles. Given the large moment of the Mn spin it can be approximated as being a classical vector for practical applications. In order to fix the parameters of the effective Hamiltonian in Eq. (A.6) in terms of the parameters of the bare Hamiltonian, we need to evaluate Eq. (A.5) for four different pairs of $|\alpha\rangle$ and $|\beta\rangle$.

A. To get T^{mm} and J^{mm}:

I. $|\alpha\rangle = |\beta\rangle = |m\sigma = \frac{1}{2}, m_s = \frac{5}{2}\rangle$:

Since Pauli's principle does not allow two identical particles with the same spin to be at the same site, applying $\hat{V}$ on $|\alpha\rangle$ or $|\beta\rangle$ will result in zero, thus from Eq. (A.5) we have $\langle\beta|\Delta|\alpha\rangle = 0$. Eq. (A.6), on the other hand, gives $\langle\beta|\Delta|\alpha\rangle = T^{mm} + \frac{5}{2}J^{mm}$.

II. $|\alpha\rangle = |\beta\rangle = |m\sigma = -\frac{1}{2}, m_s = \frac{5}{2}\rangle$:

In this case, since the hole in a given N-sp^3 orbital has opposite spin to the ones in Mn-d, applying $\hat{V}$ on $|\alpha\rangle$ or $|\beta\rangle$ will allow the hole to hop from the N-sp^3 orbital to a particular Mn-d orbital and back to the same N-sp^3 orbital. These hopping processes, furthermore, interfere constructively giving rise to a factor of 3. Hence, Eq. (A.5) yields $\langle\beta|\Delta|\alpha\rangle = -3\frac{\left|V_{\langle m,t_{2g}\rangle}\right|^2}{\Delta_E}$. Eq. (A.6), furthermore, gives $\langle\beta|\Delta|\alpha\rangle = T^{mm} - \frac{5}{2}J^{mm}$,

thus, from AI and AII we get $T^{mm} = -\frac{3|V_{\langle m,t_{2g}\rangle}|^2}{2\Delta_E}$ and $J^{mm} = \frac{3|V_{\langle m,t_{2g}\rangle}|^2}{5\Delta_E}$.

B. To get $T^{m\neq m'}$ and $J^{m\neq m'}$ (here, for instance, $m = sp^3_{N_1}$ and $m' = sp^3_{N_2}$):

I. $|\alpha\rangle = |m\sigma = \frac{1}{2}, m_s = \frac{5}{2}\rangle$, $|\beta\rangle = |m'\sigma = \frac{1}{2}, m_s = \frac{5}{2}\rangle$:

For the same reason as in AI, applying $\hat{V}$ on $|\alpha\rangle$ or $|\beta\rangle$ will result in zero, thus from Eq. (A.5) we have $\langle\beta|\Delta|\alpha\rangle = 0$. Whereas, Eq. (A.6) gives $\langle\beta|\Delta|\alpha\rangle = T^{m\neq m'} + \frac{5}{2}J^{m\neq m'}$.

II. $|\alpha\rangle = |m\sigma = -\frac{1}{2}, m_s = \frac{5}{2}\rangle$, $|\beta\rangle = |m'\sigma = -\frac{1}{2}, m_s = \frac{5}{2}\rangle$:

Like AII, applying $\hat{V}$ on $|\alpha\rangle$ or $|\beta\rangle$ will make the hole to hop from a given N-sp^3 orbital to a particular Mn-d orbital but hop back to a different N-sp^3 orbital. However, unlike AII, some hopping processes, interfere destructively giving rise to a factor of 1 instead of 3. Hence, Eq. (A.5) yields $\langle\beta|\Delta|\alpha\rangle = -\frac{\left(V_{\langle m,t_{2g}\rangle}\cdot V_{\langle t_{2g},m'\rangle}\right)}{\Delta_E}$. Whereas Eq. (A.6) gives $\langle\beta|\Delta|\alpha\rangle = T^{m\neq m'} - \frac{5}{2}J^{m\neq m'}$

Accordingly, from BI and BII we get $T^{m\neq m'} = -\frac{\left(V_{\langle m,t_{2g}\rangle}\cdot V_{\langle t_{2g},m'\rangle}\right)}{2\Delta_E}$ and $J^{m\neq m'} = \frac{\left(V_{\langle m,t_{2g}\rangle}\cdot V_{\langle t_{2g},m'\rangle}\right)}{5\Delta_E}$.

To summarize we have illustrated the effective low-energy d^5 model, specifically, we show within the 2^{nd} order perturbation theory scheme how the spin-dependent and spin-independent potentials intuitively emerge by virtually exchanging a hole between the d^5 and d^4 states.

Vita

Ryky Nelson was born and grew up in Jakarta, Indonesia. He completed his undergraduate studies at University of Indonesia in August 2007, earning a Bachelor of Science in physics. Currently, he is a candidate for the Ph.D. in physics which will be awarded in December 2015.